REPORT DOCUMENTATION PAGE

Form Approved OMB NO. 0704-0188

1. REPORT DATE (DD-MM-YYYY)	2. REPORT TYPE	3. DATES COVERED (From - To)
24-08-2017	Final Report	1-Jun-2014 - 31-May-2017

4. TITLE AND SUBTITLE
Final Report: Turbulent Flow Modification With Thermoacoustic Waves For Separation Control

5a. CONTRACT NUMBER
W911NF-14-1-0224

5b. GRANT NUMBER

5c. PROGRAM ELEMENT NUMBER
611102

6. AUTHORS

5d. PROJECT NUMBER

5e. TASK NUMBER

5f. WORK UNIT NUMBER

7. PERFORMING ORGANIZATION NAMES AND ADDRESSES
Florida State University
Sponsored Research Administration
874 Traditions Way, Third Floor
Tallahassee, FL 32306 -4166

8. PERFORMING ORGANIZATION REPORT NUMBER

9. SPONSORING/MONITORING AGENCY NAME(S) AND ADDRESS (ES)
U.S. Army Research Office
P.O. Box 12211
Research Triangle Park, NC 27709-2211

10. SPONSOR/MONITOR'S ACRONYM(S)
ARO

11. SPONSOR/MONITOR'S REPORT NUMBER(S)
64887-EG.4

12. DISTRIBUTION AVAILIBILITY STATEMENT
Approved for public release; distribution is unlimited.

13. SUPPLEMENTARY NOTES
The views, opinions and/or findings contained in this report are those of the author(s) and should not contrued as an official Department of the Army position, policy or decision, unless so designated by other documentation.

14. ABSTRACT

15. SUBJECT TERMS

16. SECURITY CLASSIFICATION OF:			17. LIMITATION OF ABSTRACT	15. NUMBER OF PAGES	19a. NAME OF RESPONSIBLE PERSON
a. REPORT	b. ABSTRACT	c. THIS PAGE			Kunihiko Taira
UU	UU	UU	UU		19b. TELEPHONE NUMBER 850-645-0140

RPPR Final Report
as of 23-Oct-2017

Agency Code:

Proposal Number: 64887EG **Agreement Number: W911NF-14-1-0224**
INVESTIGATOR(S):

Name: Kunihiko Taira
Email: ktaira@fsu.edu
Phone Number: 8506450140
Principal: Y

Organization: **Florida State University**
Address: Sponsored Research Administration, Tallahassee, FL 323064166
Country: USA

DUNS Number: 790877419 EIN: 591961248
Report Date: 31-Aug-2017 Date Received: 24-Aug-2017
Final Report for Period Beginning 01-Jun-2014 and Ending 31-May-2017
Title: Turbulent Flow Modification With Thermoacoustic Waves For Separation Control
Begin Performance Period: 01-Jun-2014 **End Performance Period:** 31-May-2017
Report Term: 0-Other

Submitted By: Kunihiko Taira Email: ktaira@fsu.edu
Phone: (850) 645-0140

Distribution Statement: 1-Approved for public release; distribution is unlimited.

STEM Degrees: 1 **STEM Participants:** 0

Major Goals: The objective of the proposed three-year study is to examine the effectiveness of high intensity acoustic waves emitted from a thermoacoustic actuator for active separation control of flow over a wall-mounted hump. A novel graphene-membrane based thermoacoustic actuator is considered as the source of acoustic waves. Carbon based materials have high conductivity which allows for extremely high power efficiency for sound generation. Furthermore, such membrane only requires alternating current to be applied, making it attractive from the point of view of implementation since the actuator can be surface-compliant with minimal weight additions. The present study will conduct large-scale three-dimensional Large-Eddy Simulations (LES) to examine the effectiveness of thermoacoustic waves to alter turbulent separated flows at $Re \approx 10^6$. The NASA hump geometry is selected as the test problem due to its extensive examination with past experiments and numerical simulations. For this problem, there has also been numerous studies with flow control using different types of actuators, such as suction and blowing, synthetic jets, and dielectric barrier discharge plasma actuators, which can be utilized to compare the performance of the currently investigated thermoacoustic actuator.

Accomplishments: We have demonstrated that the use of fundamental thermal actuation can effectively modify nonlinear dynamics in fluid flows (shear layer, flow over a hump, and airfoil wake). We started with a fundamental investigation on a free shear layer perturbed by a local periodic heating. We found that the oscillatory thermal forcing translates to hydrodynamic perturbation in the form of oscillatory surface vorticity flux and baroclinic torque at the actuation frequency in the vicinity of the trailing edge. The produced vortical perturbations can independently excite the fundamental instability that accounts for shear layer roll-up as well as the subharmonic instability that encourages the vortex pairing process farther downstream. The time-average momentum profiles are also correspondingly changed by the modification in these aforementioned nonlinear phenomena in the free shear layer. We examine the use of thermal actuation on the separated flow over a NACA 0012 airfoil at 6° angle-of-attack and chord-based Reynolds number $Re_{L_c} = 23,000$. We observe that the unsteady thermal forcing is capable of suppressing the flow separation from leading edge by triggering the roll-up of the shear layer. In 3D LES, we observe setup with a spanwise strip for the actuator is able to laminarize the flow by repetitively producing spanwise vortical structures and traps the perturbation energy in the 2D coherent structures. When a spanwise variation is introduced to the thermal actuation, we observe that the forcing can enhance the 3D mixing over the airfoil and the entrainment of free-stream momentum. The drag is significantly reduced by up to 35% accompanied by a 3.4% lift increase. The fluctuations in the aerodynamic forces are also reduced by up to 84%. With the research efforts up to date, we believe that they have provided understanding of the control mechanism with thermal-based actuation and provided a possible pathway towards flow control using actuators such as thermophones and pulse driven plasma actuators.

At the moment, we are still investigating additional forcing frequencies and spanwise wavenumbers for the thermal actuation on flow over the airfoil. Actuation effect at a higher angle-of-attack, $\alpha = 9^\circ$, will also be examined. Moreover, we propose to perform instability analyses using two different approaches in order to provide guidance to physics-based design of active flow control using thermal-based actuators.

Training Opportunities: Nothing to Report

Results Dissemination: See Section 5.3 of the uploaded report for resulting publications.

Honors and Awards: K. Taira, Office of Naval Research, Young Investigator Award, 2016.

Protocol Activity Status:

Technology Transfer: Nothing to Report

PARTICIPANTS:

Participant Type: PD/PI
Participant: Kunihko Taira
Person Months Worked: 2.00 **Funding Support:**
Project Contribution:
International Collaboration:
International Travel:
National Academy Member: N
Other Collaborators:

Participant Type: Graduate Student (research assistant)
Participant: Chi-An Yeh
Person Months Worked: 15.00 **Funding Support:**
Project Contribution:
International Collaboration:
International Travel:
National Academy Member: N
Other Collaborators:

Participant Type: Graduate Student (research assistant)
Participant: Yiyang Sun
Person Months Worked: 7.00 **Funding Support:**
Project Contribution:
International Collaboration:
International Travel:
National Academy Member: N
Other Collaborators:

Participant Type: Graduate Student (research assistant)
Participant: Aditya Gopimohan Nair
Person Months Worked: 2.00 **Funding Support:**
Project Contribution:
International Collaboration:
International Travel:
National Academy Member: N
Other Collaborators:

Participant Type: Graduate Student (research assistant)

RPPR Final Report
as of 23-Oct-2017

Participant: Phillip Michael Munday
Person Months Worked: 8.00 **Funding Support:**
Project Contribution:
International Collaboration:
International Travel:
National Academy Member: N
Other Collaborators:

Participant Type: Graduate Student (research assistant)
Participant: Muralikrishnan Gopalakrishnan Meena
Person Months Worked: 7.00 **Funding Support:**
Project Contribution:
International Collaboration:
International Travel:
National Academy Member: N
Other Collaborators:

CONFERENCE PAPERS:

Publication Type: Conference Paper or Presentation **Publication Status:** 3-Accepted
Conference Name: Ninth JSME-KSME Thermal and Fluids Engineering Conference
Date Received: 24-Aug-2017 Conference Date: 28-Oct-2017 Date Published: 27-Oct-2017
Conference Location: Okinawa, Japan
Paper Title: Thermal-based separation control of flow over an airfoil and its resolvent analysis
Authors: Chi-An Yeh, Yiyang Sun, and Kunihiko Taira
Acknowledged Federal Support: **Y**

Publication Type: Conference Paper or Presentation **Publication Status:** 1-Published
Conference Name: 55th AIAA Aerospace Sciences Meeting
Date Received: 24-Aug-2017 Conference Date: 09-Jan-2017 Date Published: 09-Jan-2017
Conference Location: Grapevine, Texas
Paper Title: Use of local periodic heating for separation control on a NACA 0012 airfoil
Authors: Chi-An Yeh, Phillip M. Munday, and Kunihiko Taira
Acknowledged Federal Support: **Y**

Final Report prepared for the US Army Research Office
Program Manager: Dr. Matthew Munson (Fluid Dynamics)

Grant: W911NF-14-1-0224

Compiled on 24 August 2017

Turbulent Flow Modification with Thermal Excitation for Separation Control

Chi-An Yeh, Phillip M. Munday, and Kunihiko Taira†

Department of Mechanical Engineering,
Florida Center for Advanced Aero Propulsion,
Florida A&M/Florida State University, Tallahassee, FL 32310, USA

Abstract

Motivated by the surging interest in the use of thermal-energy-based actuators from the active flow control community, we conduct a series of numerical investigations to uncover the underlying control mechanism of thermal-energy-based actuator and examine the control effectiveness when a fundamental thermal energy source is introduced as the only external perturbation to the flows of interest. We consider a thermal actuator model that introduces localized boundary actuation in a form of unsteady heat flux. This external thermal actuation is fed into the right-hand-side of the energy equation in the compressible Navier–Stokes equations. We study how the localized thermal forcing affects the far-field and near-field of the surrounding flow.

We start this investigation by considering a free shear layer perturbed by a local periodic heating introduced at the trailing edge of a finite-thickness splitter plate. Two-dimensional simulations are performed at the plate-thickness-based Reynolds number of 1000 without the use of subgrid-scale models. We find that thermal actuation introduces low level of oscillatory surface vorticity flux and baroclinic torque at the actuation frequency in the vicinity of the trailing edge. The produced vortical perturbations can independently excite the fundamental instability that accounts for shear layer roll-up as well as the subharmonic instability that encourages the vortex pairing process farther downstream. We demonstrate that the nonlinear dynamics of a spatially developing shear layer can be modified by local oscillatory heat flux as a control input.

Next, we leverage the findings from the thermally perturbed free shear layer and extend the employment of the thermal actuation technique to a further practical scenario in aerodynamic applications: suppression of flow separation over an airfoil. The separated flow over a NACA 0012 airfoil at 6° angle-of-attack and chord-based Reynolds number $Re_{L_c} = 23,000$ is considered as the baseline case, and a thermal actuator model is placed at the separation point to introduce unsteady thermal forcing. Both two- and three-dimensional large-eddy-simulations (LES) are employed in this investigation. The result shows that the thermal actuation is capable of suppressing boundary layer separation from the leading edge and reduce the size of the separation bubble. In 2D LES, we find that the thermal actuation locks the vortex shedding frequency onto the forcing

† Principal Investigator, ktaira@fsu.edu

frequency, reducing the drag by up to 25% with a slight decrease in lift, leading to higher aerodynamic performance (C_L/C_D) of the airfoil. The fluctuations in drag and lift are also reduced by up to 81%. In 3D LES, the thermal forcing can regularize the roll-up of the shear layer from the leading edge by chopping the shear layer into compact 2D coherent structures in a periodic manner. The development of 3D turbulent structures observed in the baseline flow can be suppressed with periodic forcing by using a 2D actuator setup (no spanwise variation). In contrast, when spanwise variation is introduced to the thermal forcing, we observe that the forcing can enhance 3D mixing over the airfoil. In both setups, the forcing is capable of reattaching the flow and reduce the size of the recirculation bubble, enabling reductions in drag and its fluctuation by up to 35% and 84%, respectively.

We show that the use of fundamental thermal input can effectively modify nonlinear dynamics in both fluid flows of interest. The advantages in applications of using thermal-based actuator for active flow control compared to other mass- and momentum-based flow actuation are also discussed. We believe that the work to date has provided a solid foundation in understanding the control mechanism of thermal-energy-based actuation and supports flow control using actuators such as thermophones and pulse driven plasma actuators.

CONTENTS

1. Introduction

Active flow control (Joslin & Miller 2009), as a multi-disciplinary research field, has been attracting great attention from different areas and exhibiting explosive growth in the past decade. As opposed to its counterpart, passive flow control, active flow control requires external energy addition to the flow. The external energy addition serves as the control input that modifies the flow of interest, and actuators play the role of passing the energy to the perturbation input that interacts with the surrounding fluid flow.

Actuator is a necessary component in active flow control. A review by Cattafesta & Sheplak (2011) discusses various types of devices used in active flow control, such as the synthetic jets (Glezer & Amitay 2002), dielectric barrier discharge (DBD) plasma actuators (Corke *et al.* 2010), and combustion powered actuators (Crittenden & Raghu 2009). The control input introduced by actuators to the flow may take the form of injection of mass, linear/angular momentum, energy, or the combination thereof, in either a steady or unsteady fashion. Among them, the introduction of thermal energy from the actuator is the main focus of this study.

The study of thermal-energy-based flow control can be traced back to the experimental investigation by Linke (1942). By taking measurements of the friction drag experienced by a heated flat plate placed transversely to the *gas* flow, he found a noticeable increase in the friction drag due to heating and attributed this increase to the accelerated laminar-turbulent transition of the boundary layer with positive heat transfer to the flow. Schlichting (1968) commented on the effect of heat transfer to the boundary layer in the aspect of inviscid instability. By introducing temperature dependence in fluid viscosity, an inflection point in the velocity profile can be introduced within the boundary layer. It follows that, for fluids whose viscosity has positive dependence on temperature (e.g. air), boundary layer can be destabilized with heat addition, and for fluids whose viscosity has negative dependence on temperature (e.g. water), boundary layer can be destabilized with heat removal. Later, Lowell & Reshotko (1974) conducted instability analysis that also takes density variations into account and arrived at the same conclusion. While other follow-up studies on external thermal forcing with spatially uniform (Lauchle & Gurney 1984; Strazisar *et al.* 1977; Zang & Hussaini 1985) and non-uniform source (Asrar & Nayfeh 1985; Strazisar & Reshotko 1978) are available for boundary-layer flows, discussions on the use of thermal forcing in other flow geometries are rarely addressed in past studies (Landrum & Macha 1987). On the other hand, examinations of the use of unsteady thermal source for flow modification are also limited in the literature (Kral & Fasel 1994).

The study by Landrum & Macha (1987) is an example of the employment of external thermal forcing on flow over an airfoil. The boundary layer over a NACA 0012 airfoil at zero-degree angle-of-attack and Reynolds number of 1.2 million is studied under the influence of a heated leading edge (first 10% of the chord), while it was the anti-icing protection that motivated their investigation. They found that, even though the turbulent fluctuation is greater with heated leading-edge, the boundary layer exhibits longer transition region than that on the airfoil without heated leading edge. With the companion stability analysis in their study, the delayed laminar-turbulent transition is attributed to the accelerated outer flow, which is not considered in the boundary layer over a flat plate. Although the use of steady heating was not for active flow control, their study has demonstrated that the characteristics of turbulent boundary layer over an airfoil can be modified by the local injection of thermal energy.

The motivation of studying the use of thermal-energy injection for active flow control is inspired by the recent developments in thermal-energy-based actuators, for which we

discuss two examples in further detail in Sections 1.1 and 1.2. Thermal-energy-based actuators rely on no mechanical moving parts. Also, the energy-based actuator has the advantage of its sheet-like arrangement that can be applied to essentially any surface, without occupying any internal space nor adding significant weight. These features are attractive to aerodynamic applications where bulkiness due to the weight and size of the actuator are undesirable, and also extend the potential use of thermal-energy-based actuators in applications including rotorcraft blades and small-scale unmanned air vehicle wings. Furthermore, since the control input is introduced only in the form of energy, thermal-energy-based actuation does not suffer the blockage effect of free-stream momentum that encountered in the use of synthetic jets (Rathay *et al.* 2014) when their spanwise spacing becomes small. With modern materials used for its main component that transfers energy to the flow, the amount of power required to deliver the control perturbation into the flow field can also be significantly reduced. Following, we provide two examples of the thermal-energy-based actuator.

1.1. *Thermoacoustic actuator*

The use of thermoacoustic actuator is motivated by the recent development of thermophone. Thermophone is a sound generation technique discovered by Arnold & Crandall. (1917). With the application of alternating current (AC) over a platinum film, they found that the Joule heating on the film periodically increases the surrounding fluid temperature and leads to local pressure fluctuations at double the frequency of alternating current. This thermophone technique was not widely utilized in the past due to the relatively large power required for a desired surface pressure disturbance level. In recent years, however, this drawback has been overcome by the use of graphene- and carbon-nanotube-based membranes for thermophones. Compared to traditional metal membranes, the carbon-based membranes can be fabricated extremely thin, usually around $\mathcal{O}(10^{-5})$ mm (Tian *et al.* 2011), such that its heat capacity per unit area (HCPUA) is at least two orders of magnitude lower than that of the metal films. Since the output power of pressure disturbance delivered to the surrounding flow field is inversely proportional to the material HCPUA, the use of carbon-based membranes dramatically enhances the device efficiency. The operating frequency is also extended in range (20 to 50 kHz) with these membranes (Tian *et al.* 2011). Considering thermophone as a new candidate for flow control actuators, the broadened range of its operating frequency is able to encompass that of many flow control applications.

Mathematical modeling for thermoacoustic actuator is also conducted by Bin *et al.* (2015) by performing analysis with uncertainty quantification. Their modeling is focused on capturing the far-field acoustics with different combinations of near-field heat transfer mechanisms. By comparing the results to experimental measurements by Tian *et al.* (2011), they showed that the characteristics of thermoacoustic actuator can be well modeled by considering only periodic heat flux to the surrounding fluid from the actuator. This finding facilitates the use of localized heat flux for the actuator model in this study, which will be discussed in Section 2.2.

One of the applications of thermophones is the author's previous numerical investigation Yeh *et al.* (2015) on utilizing a thermoacoustic actuator for control of turbulent flow over the NASA wall-mounted hump. The hump geometry is chosen from the NASA Validation Workshop for synthetic jets (Franck & Colonius 2010; Rumsey *et al.* 2006; Seifert & Pack 2002). In the study, the slot for synthetic jet is replaced by a boundary condition that models the thermoacoustic actuator. The problem setup is shown in Figure 1 with the turbulent structure visualized by Q-criterion colored with streamwise velocity. The location of the actuator is set to be at the time-averaged separation point of the

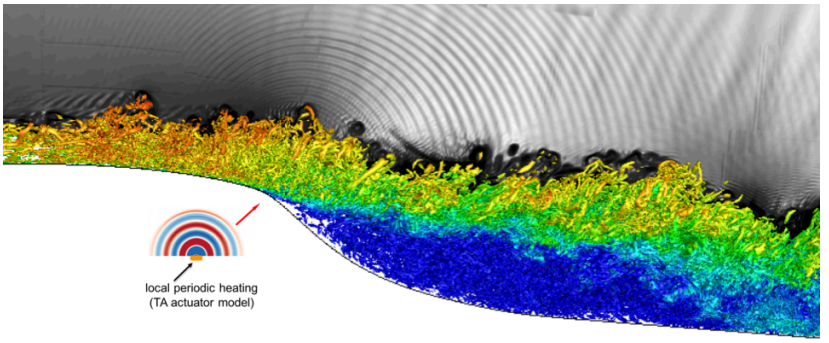

FIGURE 1. Schematic demonstration of the for thermoacoustic actuation on turbulent flow over the NASA wall-mounted hump. The slot for synthetic jet is replaced by a boundary condition that models the thermoacoustic actuator.

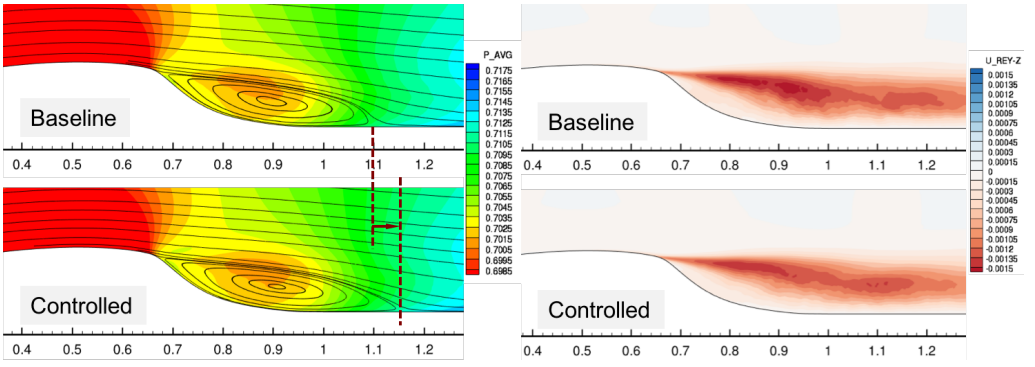

FIGURE 2. Left: The recirculation bubble visualized by time-average streamlines; Right: Spanwise Reynolds stress in the wake.

baseline flow to excite the flow at the onset of the shear layer that forms from flow separation. Large-eddy-simulations (LES) were performed for flow over a wall-mounted hump to examine the influence of thermoacoustic perturbation on reducing drag and altering the profile of the recirculation bubble. As shown in Figure 2 (right) is the spanwise Reynolds stress in the wake region, where we observe that the magnitude of Reynolds stress is decreased with control. This decrease in velocity fluctuation results in decrease momentum mixing with the high speed free stream. As a consequence, the flow reattachment is delayed and size of the recirculation bubble is increased. This change in the recirculation region can be seen in Figure 2 (left), where we observe that the streamwise extent of the bubble is increased with actuation. The thermoacoustic actuation achieves a drag reduction of 5.6% over the hump with efficient actuation power consideration, suggesting applicational potential of thermoacoustic actuation on full scale engineering problems.

1.2. *Pulse-driven plasma actuator*

On the other hand, the use of nanosecond pulse-driven dielectric barrier discharge (ns-DBD) plasma actuators for flow control has also become widespread in recent years (Lehmann *et al.* 2014; Little *et al.* 2012). The control mechanism of ns-DBD plasma actuation is believed to primarily rely on the deposition of thermal energy (Adamovich *et al.* 2012; Nudnova *et al.* 2010), in contrary to alternating current driven dielectric

barrier discharge (ac-DBD) actuator that employs electrohydrodynamic (EHD) effect to introduce momentum perturbation (Abe *et al.* 2008; Corke *et al.* 2010). For the EHD effect to be significant, the Coulomb force work introduced by the actuator needs to be in the same order of magnitude as the characteristic kinetic energy of the flow. Since the latter is significantly increased in high speed flow, the power delivered by ac-DBD plasma actuator becomes incompatible to the increased flow energy for achieving effective forcing to the flow.

The drawback of severely degraded control authority in high speed flows with ac-DBD plasma actuators has shifted some interests from ac-DBD to ns-DBD for the plasma flow control community. The pulse driven plasma actuator produces a high-energy burst in a time scale of nanoseconds. The time scale is too short for EHD effect to take place. Instead, the pulse leads to a deposition of molecular energy to the surrounding fluid and results in a localized rapid heating. Numerous studies have reported the rapid heating effect near the pulse-driven plasma actuator and attributed the kinetic mechanism of the localized heating to the energy transfer to molecular translational/rotational modes on a sub-microsecond time scale (Aleksandrov *et al.* 2010; Popov 2011). Mathematical modeling on the thermal effect has been carried out by Shkurenkov & Adamovich (2016). A recent review by Adamovich *et al.* (2017) also provides detailed discussions on how thermal perturbations are introduced by ns-DBD plasma actuator. Thus far, the community has built strong believe in the thermal mechanism on which the pulse driven plasma actuator relies through theoretical and experimental evidences.

The demonstration of the use of ns-DBD plasma actuator for separation control on an airfoil has been carried out by Little *et al.* (2012). With a spanwise strip of the pulse driven plasma actuator placed near the leading edge of an airfoil, they found that the actuation generates spanwise coherent structures at post-stall angle-of-attacks. These structures induce entrainment of the free stream momentum, thereby reattaching the separated flow to the suction surface of the airfoil. The suppression of separation also enhances the lift by over 30% compared to the baseline.

We have discussed two examples of thermal-energy-based actuators and effectiveness of their uses for (open-loop) flow control. Both cases show promising potential for full scale engineering applications. Next, we specify the scope of this study and provide an overview of the layout for the thesis.

1.3. *Overview of the present study*

This study aims to uncover the underlying control mechanism of thermal-energy-based flow actuation and examine the effectiveness of their use for flow control by only introducing thermal energy as the control input to the flow of interest. Numerous numerical simulations are performed to examine the control mechanism and control effect in detail. In Section 2, we discuss the governing equations and setups for flow simulations. More importantly, a general form of the thermal actuator model is introduced in Section 2.2 and will be used throughout this work. Section 3 examines a two-dimensional (2D) free shear layer perturbed by the thermal actuation introduced at its onset. The near-field effect of the actuator is investigated in detail to reveal how localized thermal perturbation translates to hydrodynamic perturbation that modifies the nonlinear dynamics of the shear layer formed downstream. The thermal actuation's capability to excite fundamental and subharmonic instabilities of free shear layer is also demonstrated. Section 4 capitalizes on the findings from Section 3 and extends the employment of the current thermal actuation technique to a practical scenario of aerodynamic application: suppression of flow separation over an airfoil. Concluding remarks and proposed future work to complete this thesis are discuss in Section 5.

2. Numerical approach

In this section, we discuss the flow solver and actuator model that are used throughout this study. We start the discussion with the governing equations and the flow solver setups in Section 2.1. A general form of the thermal actuator model is presented in Section 2.2. Details of the computational setup, depending on each problem in this study, is left later in Sections 3 and 4.

2.1. *Governing equations*

In this study, the compressible flow solver *CharLES* (Brès *et al.* 2017; Khalighi *et al.* 2011*a*,*b*) is used to perform both two- and three-dimensional low Mach number flow simulations. The solver utilizes a second-order-accurate finite-volume method with shock-capturing schemes and a third-order Runge–Kutta scheme for time stepping. *CharLES* is capable of performing both direct numerical simulation (DNS) and large-eddy-simulation (LES) with variety of build-in sub-grid-scale models.

CharLES solves the non-dimensional compressible Navier–Stokes equations (NSEs) in acoustic units. The governing equations are written in conservative form as

$$\frac{\partial \tilde{\rho}}{\partial \tilde{t}} + \frac{\partial}{\partial \tilde{x}_j}\left(\tilde{\rho}\tilde{u}_j\right) = 0, \tag{2.1}$$

$$\frac{\partial}{\partial \tilde{t}}\left(\tilde{\rho}\tilde{u}_i\right) + \frac{\partial}{\partial \tilde{x}_j}\left(\tilde{\rho}\tilde{u}_i\tilde{u}_j\right) = \frac{\partial}{\partial \tilde{x}_j}\left(\tilde{p}\delta_{ij}\right) + \frac{1}{Re}\frac{\partial}{\partial \tilde{x}_j}\left(\frac{\partial \tilde{u}_i}{\partial \tilde{x}_j} + \frac{\partial \tilde{u}_j}{\partial \tilde{x}_i} - \frac{2}{3}\frac{\partial \tilde{u}_k}{\partial \tilde{x}_k}\delta_{ij}\right), \tag{2.2}$$

$$\frac{\partial \tilde{e}}{\partial \tilde{t}} + \frac{\partial}{\partial \tilde{x}_j}\left[\left(\tilde{e}+\tilde{p}\right)\tilde{u}_j\right] = \frac{1}{Re}\frac{\partial}{\partial \tilde{x}_j}\left[\tilde{u}_i\left(\frac{\partial \tilde{u}_i}{\partial \tilde{x}_j} + \frac{\partial \tilde{u}_j}{\partial \tilde{x}_i} - \frac{2}{3}\frac{\partial \tilde{u}_k}{\partial \tilde{x}_k}\delta_{ij}\right)\right] + \frac{1}{RePr}\frac{\partial^2 \tilde{T}}{\partial \tilde{x}_k \partial \tilde{x}_k}, \tag{2.3}$$

with the equation of state for ideal gas:

$$\tilde{p} = \frac{\tilde{\rho}\tilde{T}}{\gamma}, \tag{2.4}$$

where γ is the specific heat ratio. The non-dimensional variables in equations 2.1 to 2.4 are the spatial coordinate $\tilde{x}_i$, time $\tilde{t}$, density $\tilde{\rho}$, velocity $\tilde{u}_i$, pressure $\tilde{p}$, energy $\tilde{e}$ and temperature $\tilde{T}$ according to the non-dimensionalization of

$$\tilde{x}_i = \frac{x_i}{L}, \quad \tilde{t} = \frac{t a_\infty}{L}, \quad \tilde{\rho} = \frac{\rho}{\rho_\infty}, \quad \tilde{p} = \frac{p}{\rho_\infty a_\infty^2}, \quad \tilde{T} = \frac{T}{T_\infty}, \quad \tilde{e} = \frac{e}{\rho_\infty a_\infty^2}, \quad \tilde{u}_i = \frac{u_i}{a_\infty},$$

where the subscript ∞ denotes the free stream condition, L is the characteristic length defined differently for each problem, and $a_\infty = \sqrt{\gamma p_\infty/\rho_\infty}$ is the free stream acoustic speed. In this work, all variables are reported in non-dimensional forms and it will be clearly stated what characteristic scales are being used for non-dimensionalization. The dimensionless parameters appearing in the governing equations are the acoustic Reynolds number and free-stream Prandtl number, given by

$$Re \equiv \frac{\rho_\infty a_\infty L}{\mu_\infty} \quad \text{and} \quad Pr \equiv \frac{\mu_\infty}{\rho_\infty \alpha_\infty},$$

where α_∞ is the free stream thermal diffusivity. We use $\gamma = 1.4$ and $Pr = 0.7$ throughout this study. Both values are representative of standard air. The value of acoustic Reynolds number, depending on the free-stream viscosity, is chosen to be $Re = 10,000$ in the free shear-layer problem in Section 3 and $Re = 76,666$ for flow over a NACA 0012 airfoil in Section 4. The temperature-varying dynamic viscosity, $\mu(T)$, is evaluated by the power law as $\mu = \mu_\infty (T/T_\infty)^{0.76}$ (Garnier *et al.* 2009). The power law models the

dynamic viscosity variation well for standard air in the range of $T/T_\infty \in [0.5, 1.7]$. This range is suitable for the current study with local thermal inputs, where we observe the temperature fluctuation is within 46% about T_∞ with the highest power of thermal actuation. In Section 4, 2D and 3D LES are performed on turbulent flow over an airfoil with Vreman sub-grid-scale model (Vreman 2004).

2.2. *Thermal actuator model*

In this study on flow control with thermal-based input, the actuator occupies a localized region on a solid boundary of the problem of interest. A model for the thermal actuator is implemented in the numerical simulations through a unsteady energy-flux boundary condition that introduces external forcing to the energy equation 2.3, along with no-slip boundary condition for the momentum equation 2.2.

In the present study, we consider two forms of actuator models. First, we consider a temporally oscillatory heat flux with zero mean as:

$$\dot{q} = \hat{q} \sin(2\pi f^+ t)\sigma(\boldsymbol{x}), \tag{2.5}$$

where the net heating input to the local fluid is zero over the forcing period. We also consider another forcing input $\dot{q}^p$ which introduces a positive direct current (DC) offset to the expression of $\dot{q}$ in equation 2.5 such that the heat flux is always positive over the duty cycle:

$$\dot{q}^p = \hat{q}\left[1 + \sin(2\pi f^+ t)\right]\sigma(\boldsymbol{x}). \tag{2.6}$$

In equations 2.5 and 2.6, f^+ and $\hat{q}$ denote the forcing frequency and amplitude, respectively, and $\sigma(\boldsymbol{x})$ provides a spatial compact support over the region where actuator is placed, whose form is dependent on each problem and will be clearly defined in Section 3 and Section 4. To quantify the forcing amplitude in each problem, we introduce the normalized total heating power from the actuator as

$$E^+ = \frac{f^+ \int_0^{1/f^+} \int |\dot{q}(\boldsymbol{x}, t)| \mathrm{d}\boldsymbol{x}\mathrm{d}t}{\frac{1}{2}\rho_\infty U_{\mathrm{ref}}^2 \cdot A U_{\mathrm{ref}}}, \tag{2.7}$$

where the numerator is the cyclic average heating power introduced by the actuator, and the denominator is the total kinetic energy flux across a characteristic area, A. We note that the values of this normalized forcing power used in this study are in the same order of magnitude ($\mathcal{O}(10^{-2})$ to $\mathcal{O}(10^0)$) of those used in plasma-based flow control works (Akins *et al.* 2015; Corke *et al.* 2010; Samimy *et al.* 2007; Sinha *et al.* 2012). Also, the maximum temperature fluctuation observed over the surface of the actuator is within 46% about the free stream temperature with the use of the largest forcing amplitude.

3. Free shear layer modification by local thermal forcing

In this section, we examine the forcing effect of local thermal forcing input on a free shear layer. In this fundamental fluid flow setup, we aim to investigate the control mechanism of thermal-based actuator. The near-field effect of the actuator is examined in detail. We found that the thermal forcing input is translated to vorticity perturbation in the near field, in the form of both surface vorticity flux and generation of baroclinic torque. This thermally-induced vortical perturbation is shown to be capable of serving as an excitation source to both the fundamental and subharmonic instabilities, which in turn modify the vortex dynamics and the spatial development of the downstream shear layer. We demonstrated that the nonlinear dynamics of a spatially developing shear layer can be modified by local oscillatory heat flux as a control input, showing applicational

potential on more complicated flow problems such as suppression of flow separation on turbulent flow over an airfoil.

3.1. *Introduction*

Shear layer may be the most common flow that arises in virtually every applications, including jets, flow over a cavity, separated boundary layer over an aerodynamic body, and merging of two streams behind the trailing edge of an airfoil. Accordingly, active control of shear layer flows has been a major area of interest for the community. Early efforts on control of shear layers arising from separated flows have been summarized by Gad-el Hak & Bushnell (1991). For jet flows, Wiltse & Glezer (1998) examined the use of dissipative-range forcing with piezoelectric actuators and found that the high-frequency actuation is able to enhance the turbulent energy cascade and increase the dissipation of turbulent kinetic energy. Later, Seifert & Pack (1999) examined the effect of synthetic jet actuation for flow control of a separated flow over a NACA 0015 airfoil and found that the actuation is able to delay stall and improve post-stall aerodynamic performance. With plasma actuators, these control effects are also observed by Post & Corke (2004) on the same airfoil. The uses of plasma actuators on other shear layer setups have been continuing to attract research interests (Akins *et al.* 2015; Corke *et al.* 2009; Samimy *et al.* 2007). Synthetic-jet-based flow control of a shear layer that forms in a separated flow over a wall-mounted hump is studied by Greenblatt *et al.* (2006), who showed control input from the jet is able to change the generation rate of turbulent kinetic energy along the shear layer. For shear layers in cavity flows, Cattafesta *et al.* (2008) summarized flow control attempts using a number of modern actuators. Flow over a backward-facing step is also a canonical problem setup where a shear layer is formed, and was chosen by Vukasinovic *et al.* (2010) to investigate high-frequency actuation effects from a spanwise arrangement of synthetic jets. While the above studies do not encompass all studies to date, they show the breadth of active control techniques being applied to shear layers that arise from a range of flows.

Amongst the aforementioned flows, the free shear layer formed by the mixing of two streams with different velocities is considered especially to be the canonical configuration for shear layer flows. Studies on the characteristics of free shear layer dates back to the seminal work of Brown & Roshko (1974), where they showed that the large spanwise roll-up coherent structures forming behind the trailing edge of a splitter plate serve as the main driving force for mixing of two streams and induce the entrainment that feeds fluid from two streams to the mixing region. Along with their work, Winant & Browand (1974) and Ho & Huang (1982) have attributed the initial shear layer roll-up to the fundamental instability waves, where as their subharmonic instability accounts for the vortex merging downstream. These findings are extended to compressible flow later by Elliott & Samimy (1990) and Clemens & Mungal (1995).

As fundamental studies on the free shear layer instabilities, Ho & Huang (1982) introduced (non-local) subharmonic velocity disturbances in the entire free streams. Bechert & Stahl (1988) found the external acoustic excitation is also able to trigger the instability wave in the shear layer. While leveraging flow instabilities is a general strategy for flow control, introducing control inputs in a limited local region may be a more practical approach than introducing control inputs externally. On the other hand, Barone & Lele (2005) studied the receptivity of the shear layer behind a finite-thickness splitter plate to various type of disturbances by performing adjoint simulations. Temperature disturbance is among one of them and the shear layer is found to be receptive to such perturbation. However, studies on the excitation of shear layer instability by directly manipulating the local temperature are limited in the literature. Based on these two

reasons, the use of a localized thermal forcing input for flow control on a free shear layer draws our interests to the present study.

The objective of this study is to assess the effectiveness of the use of local periodic heating for modifying the early evolution of a free shear layer. Two-dimensional direct numerical simulations (DNS) are performed on a spatially developing shear layer downstream a finite-thickness splitter plate, with local periodic heating introduced at the trailing edge. As it has been pointed out by Crighton (1985) and Bechert (1988), active control of shear layer by introducing control inputs downstream of the trailing edge appears ineffective, but control via manipulation of the instabilities at the onset of a shear layer can be effective. A slight perturbation during the genesis of a shear layer can lead to the overall change in flow physics downstream, because its instability characteristics determine which existing disturbances can be amplified. Nonlinear effect takes place when disturbance becomes large in magnitude and transfers energy among modes while creating new ones, which drives the evolution of the flow. Thus, focusing forcing input to the origin of a shear layer is favorable for flow control since the input can leverage the flow instabilities to grow and alter the flow behavior downstream.

In what follows, we numerically examine the capability of this thermal energy-flux-based actuation for flow control on a canonical free shear layer flow. We describe the problem and discuss the computational setup in Section 3.2. Two thermal actuator models discussed in Section 2.2 are both examined for their flow control effects. Two-dimensional baseline shear layers are characterized in Section 3.3. In Section 3.4, the underlying mechanism of how thermal actuation can introduce perturbations to the flow field and alter the characteristics of the downstream shear layer is revealed by examining the near-field effect of the actuator. The flow control effect by local periodic heating on the downstream shear layer is discussed in detail in Section 3.5. We conclude this study in Section 3.6 by offering summarizing remarks.

3.2. *Computational setup*

3.2.1. *Problem description*

We consider a two-dimensional free shear layer as a model problem to examine the effectiveness of thermal actuation. Two incoming streams, initially separated by the splitter plate, at Mach numbers $M_1 = U_1/a_\infty = 0.4$ (top) and $M_2 = U_2/a_\infty = 0.1$ (bottom) with the same free stream acoustic speed, a_∞, and pressure, p_∞, form a spatially developing shear layer from the trailing edge, as illustrated in Figure 3. Following the definition by Papamoschou & Roshko (1988), the mean convective Mach number for the shear layer is $M_c = (U_1 - U_2)\,/\,(2a_\infty) = 0.15$, with the density ratio ρ_1/ρ_2 being unity ($\rho_1 = \rho_2 = \rho_\infty$). The plate-thickness-based Reynolds number, $Re_w \equiv \rho_\infty \bar{U} w/\mu_\infty$, is set to 2500, where $\bar{U} = (U_1 + U_2)/2$ is the convection velocity, w is the plate thickness and μ_∞ is the free-stream dynamic viscosity. The boundary layers on both sides of the plate are prescribed with the same momentum thickness, θ_0, which is chosen to be 5%, 10% and 25% of the splitter plate thickness, w, resulting in the momentum-thickness-based Reynolds number $Re_{\theta_0} \equiv \rho_\infty \bar{U}\theta_0/\mu_\infty$ to range from 125 to 625.

3.2.2. *Computational approach*

The computational domain, as illustrated in Figure 3 (left), has a streamwise extent of $x/w \in [-15, 400]$ and a maximum vertical extent of $y/w \in [-200, 200]$, similar to the domain setup used by Sharma *et al.* (2011). The splitter plate has an elliptic trailing edge with eccentricity of 0.866, with its tip positioned at the origin, $x/w = y/w = 0$. The domain is discretized with a structured body-fitted mesh around the splitter

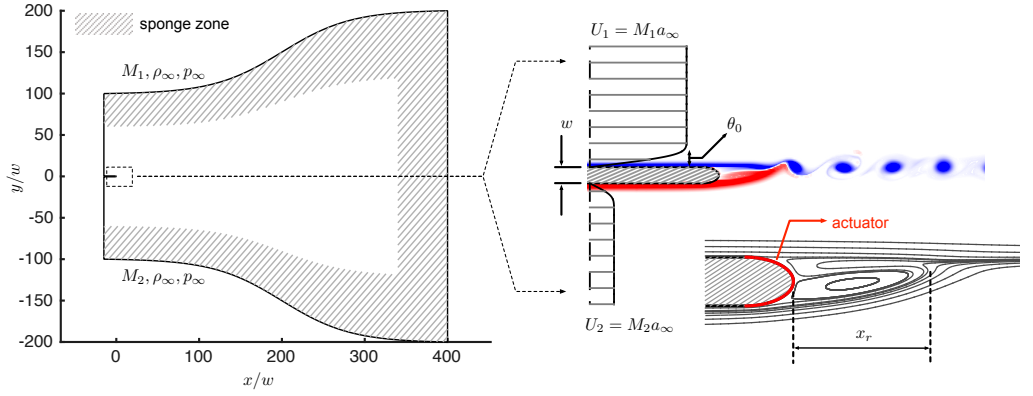

FIGURE 3. Computational setup with spatially developing shear layer downstream of a splitter plate. Two streams at free-stream Mach number $M_1 = 0.4$ (top stream) and $M_2 = 0.1$ (bottom) enter the computational domain from the inlet boundary ($x/w = -15$) on the left. Sponge zone is provided in the shaded region of the computational domain. No-slip adiabatic boundary condition is imposed over the surface of the splitter plate. For forced flow, periodic heating is introduced from the actuator placed at the elliptic trailing edge by specifying an oscillatory heat flux boundary condition at a frequency f^+.

plate. The near-wall resolution is $\Delta y^+ \equiv \Delta y u^*/\nu_\infty = 0.25$ (Choi & Moin 2012), where $u^* = \sqrt{\tau_0/\rho_\infty}$ is the wall shear velocity and τ_0 is the wall shear stress. To resolve the interaction between the shear layer and the localized periodic heat forcing, the wall-normal grid stretching rate is limited such that the Δy^+ only reaches a maximum of 1.25 within $50w$ from the wall. The overall grid size is approximately 4.4×10^5. The DNS results from this mesh were verified by comparing the flow field to that from a finer mesh, where the grid is refined in the sheared region and has the size of 6.8×10^5 grid points. No noticeable differences are found in the results from these two meshes.

Two streams are introduced to the computational domain from the inlet boundary (left) using Blasius boundary layer velocity profile. Their density profiles are computed using the Crocco–Busemann relation, with the same far-field temperature and pressure. Sponge zone (Freund 1997) is applied along the top, bottom and outlet (right) boundaries to damp out existing acoustic waves and vortical structures. The target state of the sponge zone at the top and bottom boundaries are set to $[U_1, \rho_\infty, p_\infty]$ and $[U_2, \rho_\infty, p_\infty]$, respectively. At the outlet, the time-average flow is set to be the target state of the sponge zone.

In this section, the effects of momentum thickness, the forcing frequency, and amplitude are examined in the context of modifying the characteristics of the shear layer. The flow control setup using local periodic heating and the associated input parameters are discussed below.

3.2.3. *Local periodic heating*

Both thermal actuator model from Equations 2.5 and 2.6 are used in this study. The actuator is placed over the elliptic trailing edge of the splitter plate and is implemented by specifying the spatial support function. They write

$$\dot{q} = \hat{q} \sin(2\pi f^+ t) \cos\left(\frac{\pi}{w} y\right), \quad |y| < \frac{1}{2} w; \quad \text{and} \tag{3.1}$$

$$\dot{q}^p = \hat{q}\left[1 + \sin(2\pi f^+ t)\right]\cos\left(\frac{\pi}{w}y\right), \quad |y| < \frac{1}{2}w, \tag{3.2}$$

for zero- and positive-mean forcing, respectively. For each choice of θ_0/w, the forcing frequency, f^+, is normalized by the corresponding baseline shear layer roll-up frequency, f_n, and is varied from $f^+/f_n = 0.500$ and 1.25, over which we observe forcing effects. The normalized total heating power writes

$$E^+ = \frac{f^+ \int_0^{1/f^+} \int_{|y|<\frac{w}{2}} |\dot{q}| \mathrm{d}y\mathrm{d}t}{\frac{1}{2}\rho_\infty U_{\mathrm{ref}}^2 \cdot \theta_0 U_{\mathrm{ref}}}, \tag{3.3}$$

where we use the initial momentum thickness, θ_0, as the characteristic area per unit span in this 2D study. This normalization can account for the use of higher forcing amplitude, $\hat{q}$, for thicker θ_0 for a fair comparison of forcing requirements across different θ_0, since thicker shear layer is expected to necessitate higher level of perturbation inputs to modify the shear layer. The normalized forcing power is in the range of $E^+ = 0.296$ to 2.96. The resulting maximum temperature fluctuation observed over the surface of the actuator is within 22% about the free stream temperature with the use of the largest forcing amplitude, $E^+ = 2.96$, in $\theta_0/w = 0.25$ cases.

3.3. *Baseline characterization*

3.3.1. *Shear layer characteristics*

Let us first characterize the baseline flows at three momentum thicknesses specified at the inlet: namely, $\theta_0/w = 0.05$, 0.1 and 0.25. We focus our interest in the region within the streamwise extent of $10\lambda_n$, where $\lambda_n = \bar{U}/f_n$ is the fundamental shear layer roll-up wavelength. Shown in Figure 4 are a snapshot of the normalized instantaneous spanwise vorticity (top), the velocity fluctuation magnitude (middle), and the momentum thickness profile (bottom) for the baseline flow with $\theta_0/w = 0.1$. In this work, the momentum thickness is computed using the density and streamwise velocity profiles in the shear layer as

$$\theta(x) = \int_{-\infty}^{\infty} \frac{\overline{\rho}(x,y)}{\rho_\infty} \frac{\left[\overline{u}(x,y) - U_2\right]\left[U_1 - \overline{u}(x,y)\right]}{\left(U_1 - U_2\right)^2} \mathrm{d}y, \tag{3.4}$$

where the over-bar denotes the time-averaged quantity based on the flow statistics collected over more than 200 roll-up periods. Comparing the spatial growth of momentum thickness to the instantaneous flow field, we classify the shear layer flow into three regions: (a) the shear layer roll-up region, where the momentum thickness exhibits the first rapid growth behind the trailing edge; (b) the isolated vortex region, where each formed vortex remains compact as an individual and convects closely along the centerline; (c) the vortex merging region, where the vortices start to deviate from the centerline while convecting downstream, as the initiation of the vortex merging process. This last region can be identified by the second rapid growth of the momentum thickness. These three regions can be also characterized by the streamwise change in velocity fluctuation magnitude. In regions (a) and (c), the spatial extent and the magnitude of fluctuation are both increasing, but region (b) shows no apparent changes in the growth of the momentum thickness except for the rippling variation in the momentum thickness profile. The cause of this ripple due to the orientation of the vortex evolving as the vortex convects downstream. Later in Section 3.5, the forcing effect of periodic heating on the characteristics of theses three regions are examined in further detail.

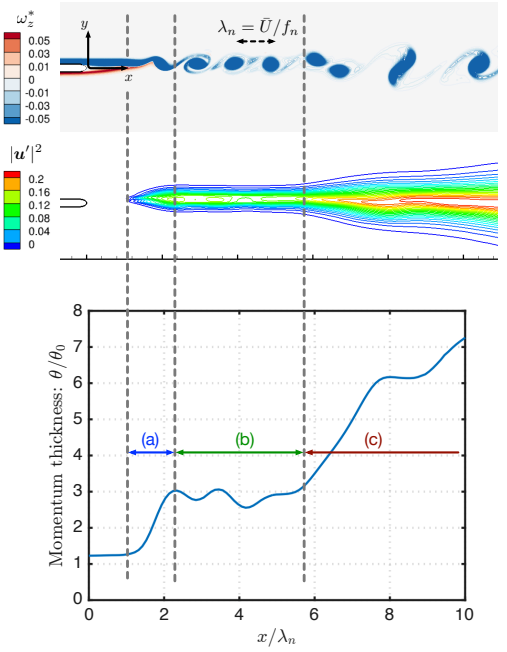

FIGURE 4. Baseline flow characterization for $\theta_0/w = 0.1$. Top: an instantaneous snapshot of normalized spanwise vorticity $\omega_z^* = \omega_z\theta_0/\bar{U}$; Middle: time-average velocity fluctuation magnitude $||\boldsymbol{u}'||^2 = (u_x'^2 + u_y'^2)/\bar{U}^2$; Bottom: spatial growth of momentum thickness (θ/θ_0). All share the same normalized streamwise coordinate, x/λ_n, where $\lambda_n = \bar{U}/f_n$ is the baseline roll-up wave length.

3.3.2. *Influence of the splitter plate thickness*

Due to the finite thickness of the splitter plate, a small recirculation region of length x_r develops directly behind the blunt trailing edge of the splitter plate, as illustrated by the time-average streamlines in Figure 3 (bottom-right). This streamline pattern for two boundary layers merging behind the trailing edge of a finite-thickness splitter plate is also observed by Sharma *et al.* (2011) and Laizet *et al.* (2010). The recirculation region can be viewed as a wake behind the finite-thickness splitter plate and result in a deficit in the profile streamwise velocity. In the theoretical study by Zhuang & Dimotakis (1995), they reported that a wake instability mode can be introduced to the shear layer which has a deficit in its streamwise velocity profile due to a wake component, and the growth rates of both the wake mode and the fundamental shear layer mode increase when the streamwise velocity profile has a greater wake deficit. Mehta (1991) experimentally showed that the splitter plate wake plays a dominant role in the development of the shear layer. The wake increases the turbulence levels in the near-field and shortens the development distance to achieve self-similarity in shear layer profiles. Remarks by Mehta (1991) on the lack of simple scaling for the shear layer with the presence of the wake also suggest that nonlinear interaction is taking place between the wake and the shear layer. Laizet *et al.* (2010) performed DNS of shear layers developing behind three different trailing edge geometries and reported that the presence of the wake can lead to different turbulent structures and shear layer spreading rate. We note, however, that there is no trace of von Kármán shedding observed in the simulations considered here, in spite of the presence of the recirculation region.

The lengths of the recirculation regions for each baseline cases with varied momentum

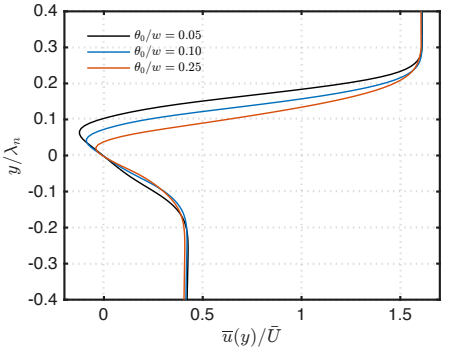

FIGURE 5. Time-average streamwise velocity profiles at $x/w = 0.3$ over y/λ_n for three baseline cases, showing stronger wake deficit for lower θ_0.

θ_0/w	x_r/w	$f_n w/\bar{U}$	St_{θ_0}	λ_n/w
0.05	4.91	0.282	0.0141	3.55
0.1	4.84	0.203	0.0203	4.92
0.25	4.60	0.112	0.0279	8.95

TABLE 1. Baseline characters of the shear layer for varied momentum thickness θ_0/w: the length of recirculation region x_r/w; roll-up frequency $f_n w/\bar{U}$; roll-up Strouhal number $St_{\theta_0} = f_n\theta_0/\bar{U}$; and roll-up wavelength λ_n/w.

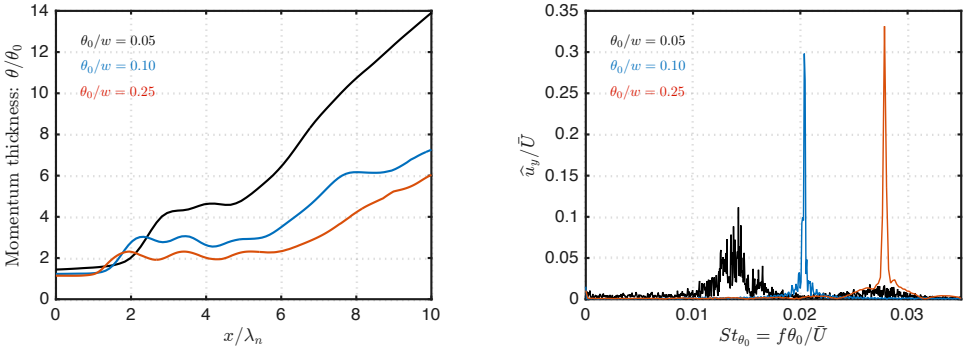

FIGURE 6. (Left) Momentum thickness growth for baseline flows with $\theta_0/w = 0.05$, 0.1 and 0.25. (Right) Transverse velocity spectra for three baseline cases at $x/\lambda_n = 2.5$. The shear layer roll-up frequency f_n for each corresponding case is determined by the peak of each spectrum.

thickness θ_0/w are summarized in Table 1, where the change in the wake length, x_r/w, is limited to 6% while θ_0/w is increased by five times. At the streamwise station of $x/w = 3.0$, the time-average streamwise velocity profile over the normalized transverse coordinate y/λ_n is presented in Figure 5. Note that the normalization of y/λ_n causes the velocity minimum to appear at different location for different choice of θ_0/w, since the value of λ_n influenced by the value of θ_0/w. In Figure 5, we observe that the wake deficit increases in both its transverse extent and maximum velocity deficit for thinner

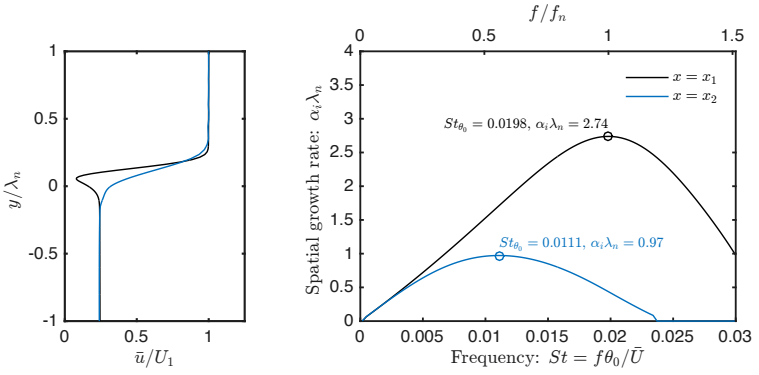

FIGURE 7. Spatial growth rates from linear stability analysis at two streamwise stations for $\theta_0/w = 0.1$ baseline. Both agree with results from DNS shown in Figure 8. Theoretical growth rates at forcing frequencies that appear in Section 3.5 are tabulated in Table 2.

incoming boundary layer. In Figure 6 we show the momentum thickness profile over the streamwise coordinate normalized by the corresponding roll-up wavelength for each case. As discussed previously using $\theta_0/w = 0.1$ for the baseline characterization, the three-region growth patterns are also observed in the other two baseline cases. The initiation of merging takes place at $x/\lambda_n \approx 6$ for all cases. However, thicker θ for the isolated vortex region and delayed roll-up are observed for thinner θ_0/w. These observations can be attributed to the stronger effect of wake when θ_0 is thinner. The effect of the plate wake can be also seen in the shear layer roll-up Strouhal number, $St_{\theta_0} = f_n\theta_0/\bar{U}$, in Table 1. We also note that the values of St_{θ_0} are lower than the prediction from linear instability theory (Ho & Huerre 1984; Monkewitz & Huerre 1982), $St_{\theta_0} = 0.032$, in all baseline cases. This also suggests that the effective initial momentum thickness is thicker than that on the high speed side, θ_0, because of the presence of the wake. Therefore, for thinner θ_0 where the wake effect is more pronounced, the greater deviation of St_{θ_0} from 0.032 is observed. The stronger wake effect on thin θ_0 can also be inferred from Figure 6, where the transverse velocity spectra at $x/\lambda_n = 2.5$ for three baseline cases are shown. The clean peaks in the cases of $\theta_0/w = 0.1$ and 0.25 suggest a synchronized shear layer roll-up and shedding, whereas the cause of the less prominent peak and broader frequency content in the case of $\theta_0/w = 0.05$ can be attributed to the nonlinear interaction between the shear layer roll-up mode and the wake mode that redistribute the energy of the roll-up frequency to other nearby frequencies.

3.3.3. *Local stability analysis*

To determine regions with linear growth of perturbation and predict the corresponding growth rate for the Kelvin–Helmholtz instability, local linear spatial stability analysis on the baseline flow is also performed at the onset region and the isolated vortex region of the shear layer. We compute the corresponding spatial growth rate at a specified perturbation frequency using the time-average density and streamwise velocity profiles as the base flow for the compressible Rayleigh equation (Sabatini & Bailly 2014).

Figure 7 shows the stability analysis results for $\theta_0/w = 0.1$ baseline flow. Time-average flow profiles at two streamwise stations (shown on the left) are chosen about which to perform the instability analysis. The first station x_1, corresponding to $(x_1 - x_r)/\lambda_n = 0.24$ or $x_1/\lambda_n = 1.22$, is located slightly downstream of the recirculation region but

	$x = x_1$			$x = x_2$	
f^+/f_n	1.00	1.16	1.25	0.500	0.575
$\alpha_i \lambda_n$	2.74	2.50	2.22	0.931	0.942

TABLE 2. The theoretical spatial growth rates obtained at forcing frequencies appearing in Section 3.5 at stations $x = x_1$ and x_2. These values of growth rates will be compared to the growth rates of forcing mode later in Figures 12 and 18.

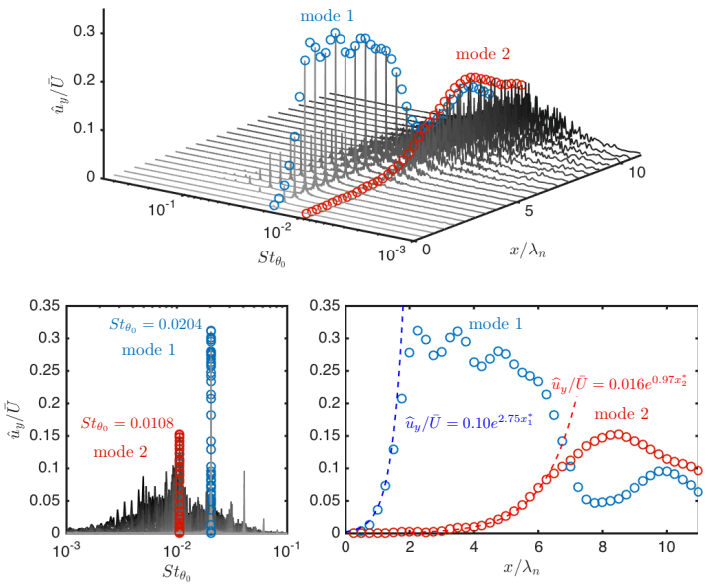

FIGURE 8. Transverse velocity spectra over the centerline: (top) the spatial development of spectra; (bottom-left) view from amplitude-frequency plane; (bottom-right) streamwise profiles of modal amplitudes for roll-up and merging mode with fitted exponential growth functions, where $x_1^* = (x - x_1)/\lambda_n$ and $x_2^* = (x - x_2)/\lambda_n$. The frequencies and growth rates of mode 1 and mode 2 agree with linear stability theory prediction in figures 7 with less than 3% differrence.

upstream of the shear layer roll-up region. In Figure 4, the station $x_1/\lambda_n = 1.22$ is located in the flat region before the first sudden growth of the momentum thickness. Similarly, we choose the second station x_2, where $(x_2 - x_r)/\lambda_n = 3.1$ or $x_2/\lambda_n = 4.06$, in the isolated vortex region indicated by the second flat region and before the second sudden growth. In Figure 7, the most amplified frequencies and the corresponding spatial growth rates are $St_{\theta_0} = 0.0198, \alpha_i \lambda_n = 2.74$ and $St_{\theta_0} = 0.0111, \alpha_i \lambda_n = 0.97$ for stations $x = x_1$ and $x = x_2$, respectively. We compare these values to the results from DNS shown in Figure 8. In the top sub-figure, the spectra of transverse velocity is plotted over a series of streamwise locations. The symbol ○ (referred to as mode 1 hereafter) represents the first spatially amplified mode and ○ (referred to as mode 2 hereafter) depicts the second mode. Their corresponding frequencies in terms of Strouhal numbers are $St_{\theta_0} = 0.0204$ and 0.0108 for modes 1 and 2, respectively, as captured in the bottom-left figure. Compared to the frequencies predicted by linear stability theory, the differences are only approximately 1.5% and 3% for the modes 1 and 2, respectively. The spatial growth of the modal amplitude can be seen in bottom-right subplot of Figure 8. Also, in the bottom-right

figure, the amplitude growth of the modes 1 and 2 are fitted with exponential growth function in $0 \leqslant x/\lambda_n \leqslant 1.6$ and $2.5 \leqslant x/\lambda_n \leqslant 5.5$, respectively for each mode. We also find the growth rates $\alpha_i \lambda_n$ from the fitting differ only by 0.7% and 2% from the prediction of the linear theory for roll-up and merging modes, respectively. The fitted function deviates from the simulation data ○ and ○ past $x/\lambda_n = 1.5$ and 6.5, respectively. These deviations are expected since, referring to Figure 4, these two stations have already reached the vortex formation and merging regions where momentum thickness exhibits a sudden streamwise growth and the parallel flow assumption is no longer valid.

The agreement between the results from DNS and the linear stability analysis on the baseline flow provides deep insight into the growth of perturbations in the aforementioned regions. As we discuss later, the frequencies in the vicinity of that of mode 2 are also considered as candidates for the actuation frequency of the local periodic forcing in Section 3.5. The growth rate prediction at the forcing frequency will also be compared to the forced cases later in discussions related to figures 12 and 18.

3.4. *Thermal control mechanism*

In this section, the local effects of periodic thermal forcing is studied to understand how the thermal perturbations give rise to hydrodynamic perturbations and modifies the shear layer physics downstream. The local temperature fluctuation and surface pressure disturbance introduced by local periodic heating change local vorticity flux through the solid boundary, either by changing the surrounding fluid properties or wall-tangential pressure gradient (Hornung 1989; Wu & Wu 1993). The fluctuations in pressure and density in the vicinity of the actuator may also generate volumetric baroclinic vorticity, $(\nabla\rho \times \nabla p)/\rho^2$. In this two-dimensional study, we evaluate the local wall-normal vorticity flux using (Wu & Wu 1993)

$$\sigma_z(s) = -\frac{1}{\rho_0(s)} \left\{ \hat{\boldsymbol{e}}_n(s) \cdot \boldsymbol{\nabla} \left[\mu(s)\, \omega_z(s) \right]_0 \right\}, \tag{3.5}$$

where μ and ω_z are the dynamic viscosity and spanwise vorticity, respectively, subscript 0 denotes the wall adjacent quantities, s is the spatial parameter describing the splitter plate surface, and $\hat{\boldsymbol{e}}_n$ is the unit wall-normal vector. In two-dimensional Cartesian coordinates, the baroclinic torque generation is computed using

$$B_z(x,y) = \frac{1}{\rho^2} \left(\frac{\partial \rho}{\partial x}\frac{\partial p}{\partial y} - \frac{\partial \rho}{\partial y}\frac{\partial p}{\partial x} \right). \tag{3.6}$$

These two quantities from the baseline and forced flows are examined below.

Without loss of generality, we consider the case with $\theta_0/w = 0.1$. The two quantities in Equations 3.5 and 3.6 for the baseline and forced flows are examined to quantify their fluctuation magnitudes and frequencies. The forced and baseline computations are started at $tf_n = 0$ from the same initial condition, which is associated with the instantaneous baseline flow with steady flow statistics. For the forced case, periodic heating at the trailing edge is turned on at $tf_n = 0$ using Equation 3.1 with $f^+/f_n = 0.500$ and amplitude of $E^+ = 0.741$. Flow statistics are collected over $tf_n \in [100, 250]$.

The change in these two quantities between the forced and baseline cases is shown in Figure 9, where $\sigma^*_{z,\mathrm{rms}} = \sigma_{z,\mathrm{rms}}/\Omega_z$ is the root-mean-square value of σ_z, normalized by $\Omega_z = \int_{y\in\mathbf{inlet}} \omega_z \boldsymbol{u} \cdot \hat{\boldsymbol{e}}_n \mathrm{d}y$, namely, the total Euler flux of vorticity introduced by two inlet boundary layers. Similar normalization is used for $B^*_{z,\mathrm{rms}}$. We observe that both of these quantities exhibit higher fluctuation magnitudes in the thermally forced flow. Furthermore, note that the maximum magnitude of $B^*_{z,\mathrm{rms}}$ in the vicinity of the actuator is $O(10^2)$ compared to the baseline flow. As reported by Cheung & Lele (2009), the

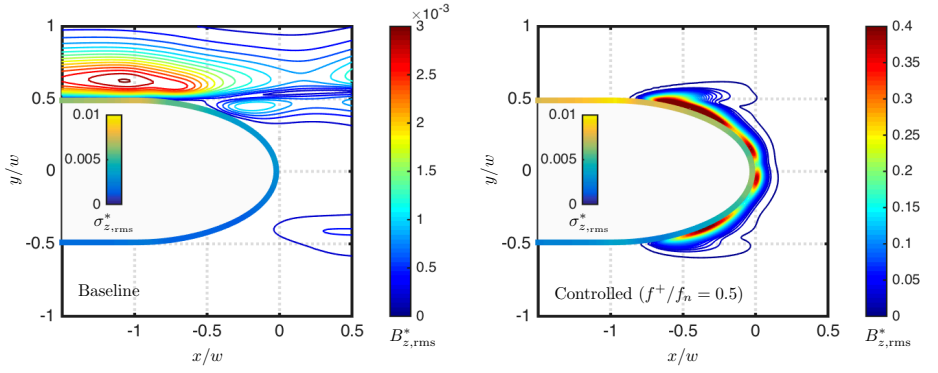

FIGURE 9. Fluctuation magnitudes of spanwise vorticity flux over the plate surface, $\sigma^*_{z,\mathrm{rms}}$, and volumetric baroclinic torque generation rate, $B^*_{z,\mathrm{rms}}$, of the baseline (left) and forced ($f^+/f_n = 0.500$, right) flows. Both quantities exhibit higher levels of fluctuations in the controlled case.

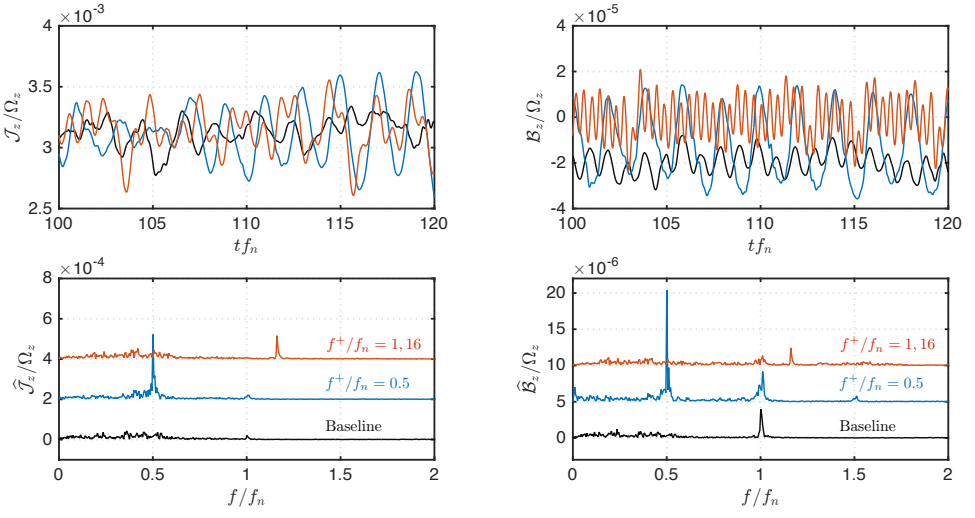

FIGURE 10. Temporal oscillations (top) and their frequency spectra (bottom) for total vorticity flux $\mathcal{J}_z$ (left) over the trailing edge, and total volumetric baroclinic torque generation, $\mathcal{B}_z$ (right) near the trailing edge. Measurements from the baseline and two forced ($f^+/f_n = 0.500$ and $f^+/f_n = 1.16$) flows are presented. In the control cases, both $\widehat{J}_z/\Omega_z$ and $\widehat{B}_z/\Omega_z$ have a prominent peak at the forcing frequency. The spectra are shifted vertically for graphical clarity.

baroclinic vorticity generation plays an important role in governing shear layer dynamics, especially for subsonic shear layers. In their study, the order of magnitude difference between a heated (free-stream temperature ratio of 1.5) and an unheated (with the same free-stream temperature) shear layer is also of $O(10^2)$. The additional generation of baroclinic vorticity takes part in the vortex dynamics in the heated shear layer and leads to different behaviors from the unheated shear layer.

We compute the total vorticity flux over the trailing edge as

$$\mathcal{J}_z = \int_{s\in\text{tip}} \sigma_z(s)\mathrm{d}s \tag{3.7}$$

and the total baroclinic generation near the trailing edge as

$$\mathcal{B}_z = \int_{|\boldsymbol{r}|<2w} B_z(\boldsymbol{r})\mathrm{d}v. \tag{3.8}$$

The quantities $\mathcal{J}_z$ and $\mathcal{B}_z$ are normalized by Ω_z and plotted in Figure 10 over time and frequency domains. As observed from the frequency domain, both of these quantities peak at the forcing frequencies, suggesting the fluctuations in $\mathcal{J}_z$ and $\mathcal{B}_z$ are indeed induced by the local periodic forcing.

The present flow control technique utilizes local periodic heating as an energy-deposition-based forcing, which introduces additional generation of vorticity. As vorticity quantifies the rotation of fluid particles, we may also consider the present technique as a vorticity-based forcing, in contrast to other momentum-based flow control techniques such as synthetic jets (Glezer & Amitay 2002). When the extra oscillatory vorticity is introduced to the shear layer at its onset, it can trigger the instability responsible for the shear layer roll-up, or modify the strength of each vortex formed from shear layer roll-up and change their interaction dynamics downstream.

3.5. *Flow control effects on the shear layer*

In this section, the influence of the forcing frequency (f^+) and the forcing type ($\dot{q}$ and $\dot{q}^p$) on the shear layer is examined. Each DNS is initialized with an instantaneous flow field from the baseline flow, with steady statistics based on at least 300 fundamental roll-up periods. Forcing is turned on from this initial condition. Flow statistics for the controlled flows are collected after 100 roll-up periods. The reported controlled flow spectrum and mean-flow-based momentum thickness are evaluated over at least another 200 roll-up periods. We start the discussion with the use of $\dot{q}$ in Sections 3.5.1 and 3.5.2. Forcing with $\dot{q}^p$, which is $\dot{q}$ with a positive direct current (DC) offset, is examined in Section 3.5.3.

3.5.1. *Spreading enhancement ($f^+ \approx 0.5 f_n$)*

We examine the forcing effect when the actuation frequency is close to the first subharmonic of the roll-up frequency with the use of $\dot{q}$. Two forcing frequencies are examined: namely, $f^+/f_n = 0.575$ and 0.500. The forcing frequency $f^+/f_n = 0.575$ is selected for being close to the frequency of mode 2 found in Figure 8. The exact first subharmonic $f^+/f_n = 0.500$ is also chosen. For fair comparison, all cases presented in this section are based on the same forcing power of $E^+ = 0.741$. In the discussions below, we first highlight the common forcing effects for these two forcing frequencies. We then discuss the differences between the two forced cases.

We start our detailed discussion on cases with $\theta_0/w = 0.1$. The baseline and forced flows are compared in figures 11 and 12. It is found that the forcing is able to change the vortex dynamics by encouraging the merging downstream while keeping the momentum thickness unchanged in the region dominated only by fundamental roll-up. We first track the center of each individual vortex after roll-up using the Q-criterion. By tracking all formed vortices over a time span of 100 roll-up periods, we visualize the vortex trajectories by black transparent dots and the contour lines for a representative instantaneous spanwise vorticity field in Figure 11 (left). Observing the trajectories, it is clear that,

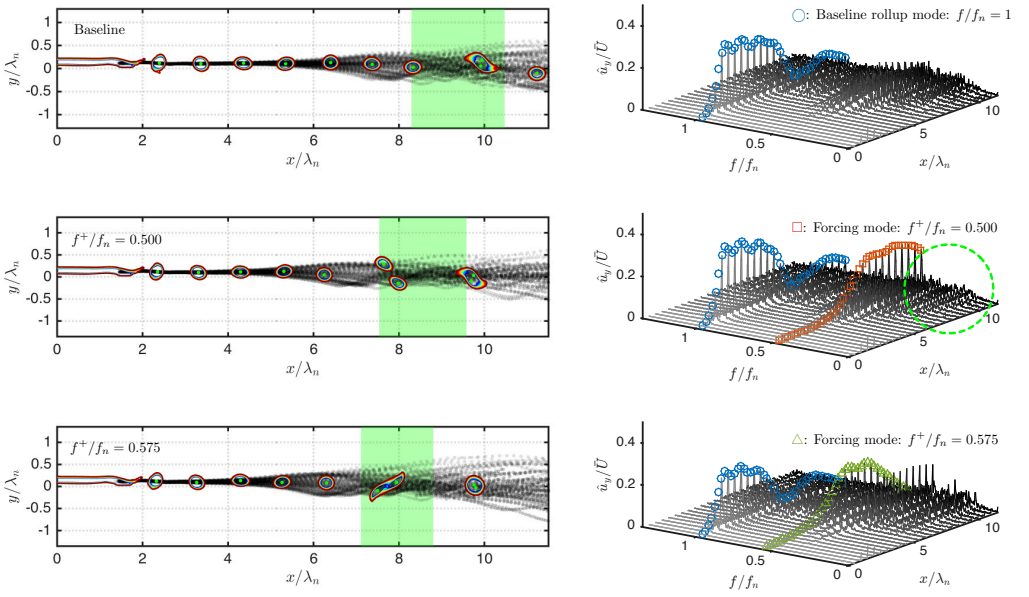

FIGURE 11. Vortex trajectories (left) and modal amplitude evolution (right) for $\theta_0/w = 0.1$. The merging location and its spatial variation is depicted by the green-shaded region (left) for each case. The forcing mode for $f^+/f_n = 0.500$ maintains its high level of modal amplitude while marching downstream, and suppresses other lower frequency modes to grow, as highlighted by the cleaner spectra in the green circled region.

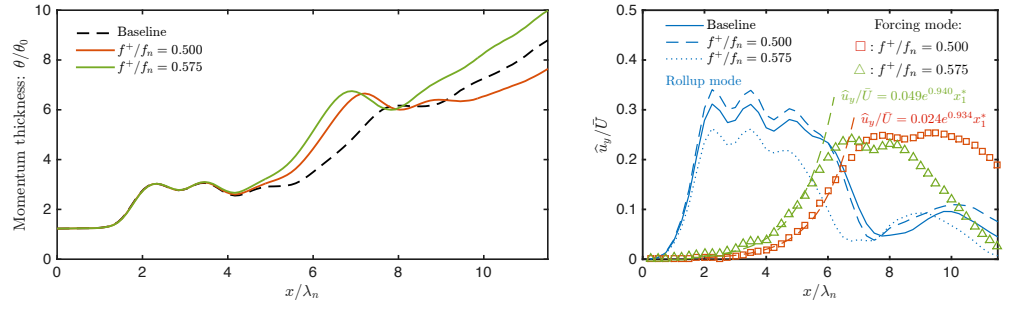

FIGURE 12. Momentum thickness growth (left) and modal amplitude evolution (right) for $\theta_0/w = 0.1$ with forcing frequency close to the first subharmonic of f_n.

as the vortices convect downstream, they spread away from the centerline ($y/\lambda_n = 0$) earlier upstream in the forced flows compared to the baseline case. This deviation from the centerline serves as an initiation for vortex merging process (Ho & Huang 1982; Winant & Browand 1974). While the vortex merging process takes place, the flow passes through a stage where a pair of vortices become vertically aligned, which then results in the steep spatial growth of the momentum thickness. For example, the controlled case with $f^+/f_n = 0.500$ shows the vertical alignment to take place at $x/\lambda_n \approx 7$. By observing the momentum thickness in Figure 12 (left), we find that this steep growth

indeed corresponds to where the trajectories demonstrate deviation from the centerline for each case. With forcing at these two frequencies, the momentum thickness does not exhibit any change to that of the baseline until this second growth takes place farther upstream compared to the baseline.

A merging criterion is set up such that two vortices are considered to be merged if their instantaneous mutual distance is less than $0.2\lambda_n$. By setting this threshold , we show the average streamwise location along with the variation (standard deviation) of where merging takes place by the green-shaded regions for each case in Figure 11 (left). Again, by comparing the shaded region from the forced cases with the baseline, it is found that the merging process completes upstream with reduced spatial variation. Observation made from the vortex tracking and mean flow momentum thickness both enable us to draw the conclusion that the forcing is able to change the vortex dynamics by encouraging the merging downstream while keeping the momentum thickness unchanged in the region dominated only by fundamental roll-up.

Since the vortex merging process is dominated by the subharmonics of the roll-up frequency, we now examine the flow over the frequency domain and focus on low frequency components with $f/f_n \leqslant 1$. The transverse velocity spectra along the centerline are shown in Figure 11 (right) for each corresponding case on the left. Comparing the forced cases to the baseline case, we find that the forcing mode in each forced case is amplified downstream, which suggests that both control inputs ($f^+/f_n = 0.500$ and 0.575) are efficiently leveraging the shear layer instability. Moreover, the growth rates of these two forcing modes are both well predicted by the local stability analysis as previously depicted in Figure 7. The energy distribution among the spectra does not show noticeable change from the baseline case until these two forcing modes start to be amplified at $x/\lambda_n \approx 4$, as shown in Figure 11. As discussed in Section 3.3.3, this streamwise station is in the isolated vortex region with linear perturbation growth. This location also corresponds to where momentum thickness starts to depart from that of the baseline with forcing, as seen in Figure 12 (left). The excited low-frequency instability wave induced by the periodic heating accelerates the emergence of the vortex merging process within the shear layer. This observation agrees with those from the experimental study by Ho & Huang (1982) and the numerical simulation by Kourta *et al.* (1987).

Next, we shift our attention to the difference between forcing effects with $f^+/f_n = 0.575$ and 0.500. In Figure 11 (left), even though in both forced cases the vortex starts to deviate from centerline earlier than it does in baseline flow, the deviation takes place earlier for the $f^+/f_n = 0.575$ case than the $f^+/f_n = 0.500$ case. Correspondingly, the merging location is also farther upstream with $f^+/f_n = 0.575$. Moreover, the second growth in momentum thickness is also taking place earlier with $f^+/f_n = 0.575$ as shown in Figure 12 (left). Such observations can be explained by the greater growth rate in the forcing mode that both predicted by stability analysis and exhibited in Figure 12 (right). The vortex merging process takes place in a more repetitive manner when forcing is introduced at the frequency with higher growth rate, leading to a lower variation in the vortex merging location visualized by the narrower green shaded region for $f^+/f_n = 0.575$. By observing all merging process identified by our criterion and examining all collected flow field snapshots, we find 17% of vortices are not paired with any other vortices with $f^+/f_n = 0.500$, whereas there are only 13% of vortices not going through pairing process $f^+/f_n = 0.575$ in the streamwise window of $x/\lambda_n < 14$.

After the vortices undergo merging, on the other hand, vortex trajectories exhibit less vertical variation in the subharmonic forced case than they are in the case with $f^+/f_n = 0.575$. These observations also agrees with those in the development for momentum thickness. The θ/θ_0 profiles also appears to be thinner for $x/\lambda_n > 8$ for

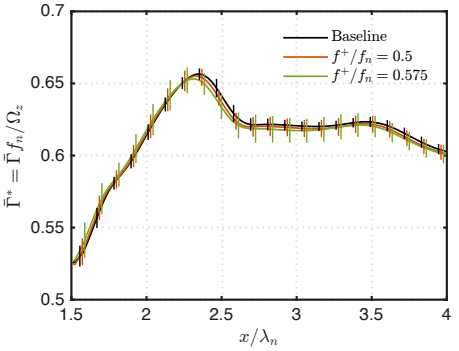

FIGURE 13. Normalized ensemble averaged vortex circulation ($\bar{\Gamma}^*$) and its variation (vertical bars) for cases of $\theta_0/w = 0.1$. We normalized the average circulation, $\bar{\Gamma}$, by the characteristic vorticity that is fed to each vortex in the roll-up period, Ω_z/f_n, from two streams. Low frequency forcing does not significantly change the mean strength but introduces greater variation in the strength of each vortex.

the case with $f^+/f_n = 0.500$. By examining the spatial evolution of spectra in figures 11 (right) and 12 (right), we find that, even though the amplitude decay in roll-up mode takes place upstream compared to the baseline case for both forced cases, the $f^+/f_n = 0.500$ case shows a faster decay rate than $f^+/f_n = 0.575$ case does. The forcing mode for $f^+/f_n = 0.500$ maintains its high level of modal amplitude while marching downstream, and suppresses other lower frequency modes to grow, as highlighted by the cleaner spectra in the green circled region compared to those of both baseline and $f^+/f_n = 0.575$ cases in Figure 11 (right). This reduction is due to the lower spillage from the modal energy at the forcing frequency. Since the growth of other low frequency modes keeps the shear layer to spread downstream, the relatively flat region in momentum thickness in subharmonic forced case can also be attributed to the absence of these lower frequency modes, as shown in Figure 12 (left).

As pointed out in Section 3.4, the thermal actuation can produce oscillatory vorticity flux over the trailing edge. This extra fluctuating vorticity generation is in turn fed to each formed vortex and leads to the variation in its strength from one vortex to another. This is shown in Figure 13, where normalized circulation at each streamwise station is averaged over each formed vortex. We observed that, in both forced cases, the mean vortex strength does not significantly change from that of the baseline, but the variation in strength is larger. The variation in vortex strength can tip over the spatial balance from one vortex to another, resulting in its trajectory deviation from the centerline. The spread of shear layer can be attributed to both the random trajectory deviation and vortex merging process. As the strength variation in $f^+/f_n = 0.575$ is greater than $f^+/f_n = 0.500$, the trajectory deviation and merging are indeed taking place earlier for $f^+/f_n = 0.575$ than for $f^+/f_n = 0.500$.

The forcing effects with $f^+/f_n = 0.500$ and 0.575 in cases of initial momentum thicknesses, $\theta_0/w = 0.05$ and 0.25 are qualitatively similar to cases of $\theta_0/w = 0.1$ discussed above. We find noteworthy effects with subharmonic forcing using $\hat{q}$ in the case with $\theta_0/w = 0.25$, as shown in Figure 14 (left). Even though the vortex starts to deviate from the centerline earlier in both of the forced cases compared to the baseline, the vortex merging process takes place in a more repetitive (locked) manner when forcing is introduced at the first subharmonic of the roll-up frequency. The ordered and repetitive trajectories in $f^+/f_n = 0.500$ leaves a white region absent of any trajectories around

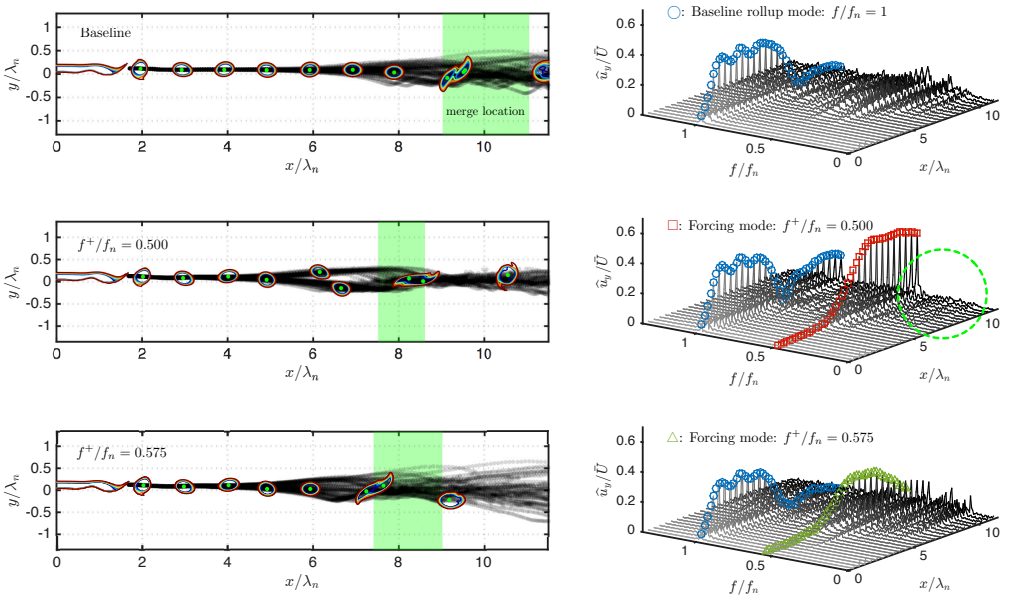

FIGURE 14. Vortex trajectories (left) and modal amplitude growth (right) for the $\theta_0/w = 0.25$ cases. The merging location and its spatial variation is depicted by the green-shaded region (left) in each case.

$x/\lambda_n \approx 6.5$, where no vortices have traveled through. The use of subharmonic frequency allows for vortex merging by successive pairs along the vortex train. Also, after merging, vortex trajectories show significant reduction in their variations in the subharmonic forced case than in the $f^+/f_n = 0.575$ case. The growths of the modal amplitudes is shown in Figure 15 (bottom), where the modal amplitudes at both forcing frequencies are amplified downstream. The modal amplitude at the forcing frequency in $f^+/f_n = 0.500$ case maintains its high level while marching downstream, and suppresses other lower frequency modes to grow, as highlighted by the clean spectra in the green circled region, compared to the baseline and $f^+/f_n = 0.575$ cases in Figure 14 (right), due to reduced spillage of the modal energy at forcing frequency. Since the growth of other low frequency modes keeps the shear layer spreading downstream, the slower growth in θ, as shown in Figure 15 (top) for both θ_0 cases, can also be attributed to the absence of these lower frequency modes.

3.5.2. *Excitation of fundamental roll-up ($f^+ \approx f_n$)*

Let us discuss the forcing effects when the forcing frequency is close to f_n with the use of $\dot{q}$ (Equation 3.1). We consider forcing frequencies of $f^+/f_n = 1.0$, 1.16 and 1.25 with $\theta_0/w = 0.1$ and $\theta_0/w = 0.05$. All cases presented in this section are of the same forcing power of $E^+ = 0.741$. Although we have also studied forced flow with forcing frequency up to $f^+/f_n = 16$, no significant change in the forced two-dimensional shear layer is observed for cases with $f^+/f_n \geqslant 2$.

Shown in Figure 16 is the transverse velocity spectra for the baseline and forced cases with $f^+/f_n = 1.00$, 1.16 and 1.25 at a streamwise station of $x/\lambda_n = 3$ on the centerline. As discussed in Section 3.3, the stronger wake effect in $\theta_0/w = 0.05$ baseline flow leads to

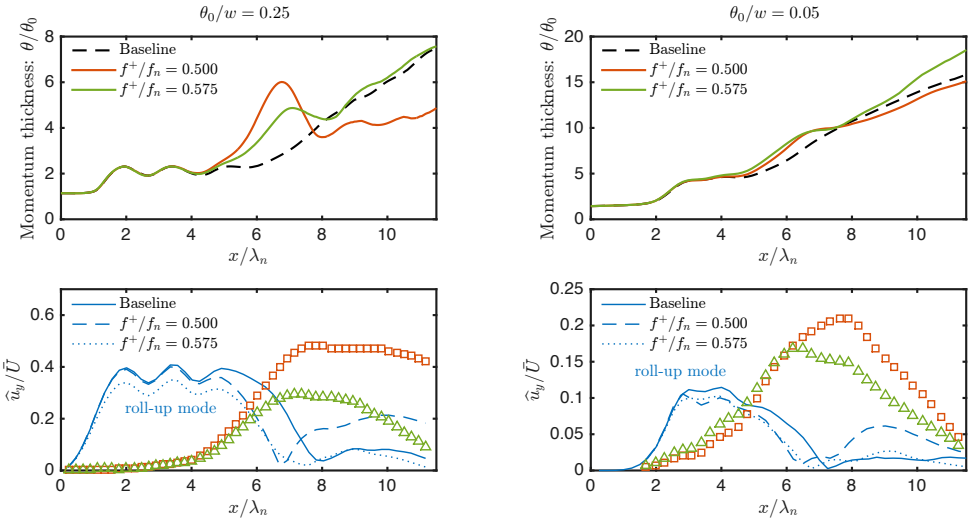

FIGURE 15. Momentum thickness growth (top) and modal amplitude growth (bottom) with low-frequency forcing. Cases with $\theta_0/w = 0.25$ (left) and $\theta_0/w = 0.05$ (right). In bottom figures, □. represents forcing mode for $f^+/f_n = 0.500$ and ○ represents $f^+/f_n = 0.575$.

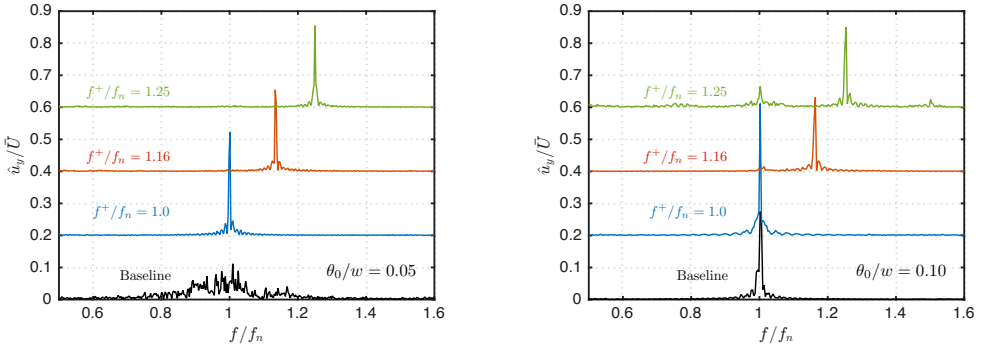

FIGURE 16. Transverse velocity spectra at $x/\lambda_n = 3.0$: Shedding is observed to lock onto the forcing frequency when $f^+/f_n \in [1.00, 1.25]$. (Left) $\theta_0/w = 0.05$; (Right) $\theta_0/w = 0.1$. The spectra are shifted vertically for graphical clarity.

a less synchronized shear layer roll-up and a spectrum with broader distribution of energy across frequencies. With periodic heating at frequencies considered here, we find that the forcing is able to lock the roll-up onto the forcing frequency, indicated by the prominent peaks at the corresponding forcing frequency for each case for both $\theta_0/w = 0.05$ and 0.1 in Figure 16.

Analogous to the discussion for low-frequency forced cases, in figures 17 and 18 we show the vortex trajectories and spatial revolution of transverse velocity spectra and momentum thicknesses for baseline and three forced cases. The thermal forcing input serves as an excitation to the fundamental instability wave and encourages the shear layer roll-up at the forcing frequency. In cases with $f^+/f_n = 1.0$ and 1.16, the thermal forcing results in the earlier shedding than that of the baseline. This can be seen by

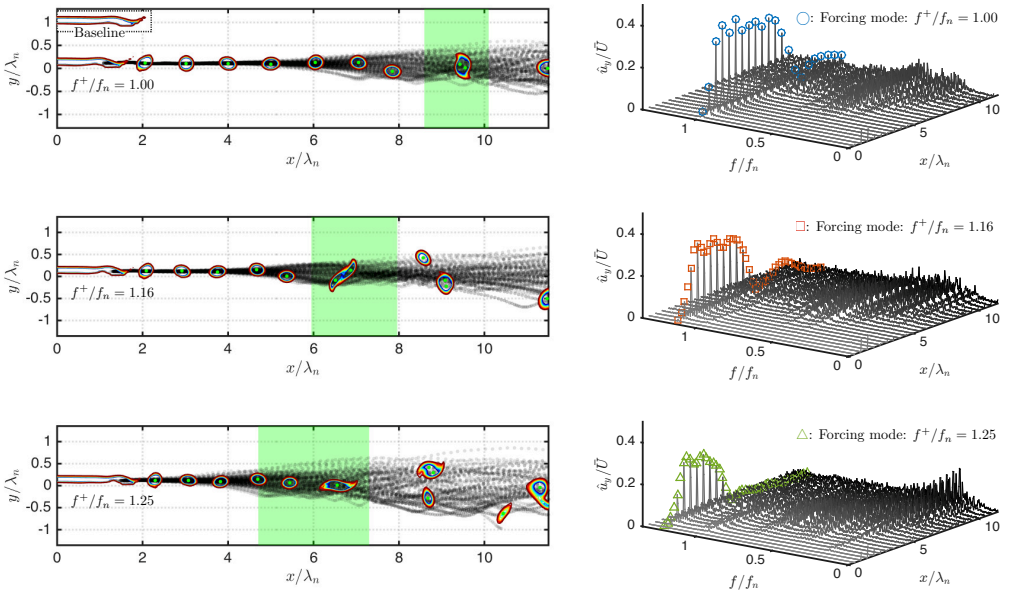

FIGURE 17. Vortex trajectories (left) and modal amplitude growth (right) for $\theta_0/w = 0.1$ cases. With f^+ close to f_n, the forcing is able to excite the shear layer roll-up and accelerate the roll-up process.

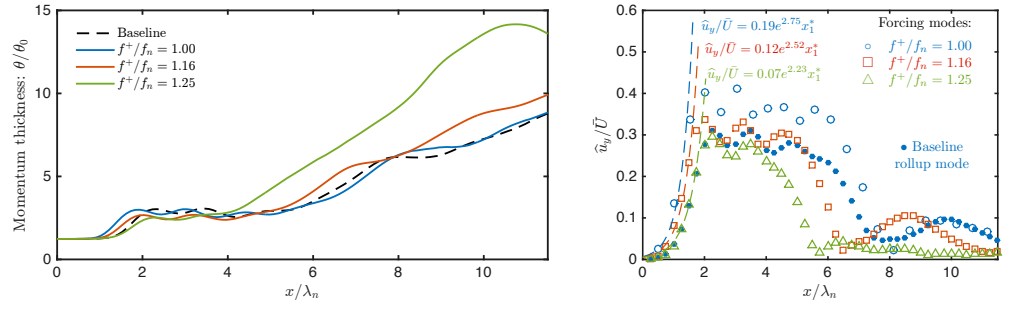

FIGURE 18. Momentum thickness growth (left) and modal amplitude growth (right) for cases with $\theta_0/w = 0.1$ and $f^+/f_n = 1.0$,1.16 and 1.25.

comparing the instantaneous vorticity contours in the initial shedding region: in both cases of $f^+/f_n = 1.0$ and 1.16, the vorticity sheet formed from $x/\lambda_n = 0$ start to carry streamwise instability wave earlier than the baseline. Earlier roll-up can also be identified from the first rapid growth of θ/θ_0 in Figure 18 (left).

With $f^+/f_n = 1.0$, the synchronized shear layer roll-up due to forcing can also be observed from the uniform spacing between each vortex in the vortex train, as show in Figure 17 (left). Also, the forcing is able to suppress the vortex deviating from the centerline. This leads to an extended isolated vortex region with forcing, suggested by the wider flat region in $1 \leqslant x/\lambda_n \leqslant 5$ in Figure 18 (left).

The spatial development of the frequency spectra and the modal amplitude growth are shown in figures 17 (right) and 18 (right), respectively. For the three forced cases, the amplitudes of the modes with their frequencies corresponding to the actuation frequencies

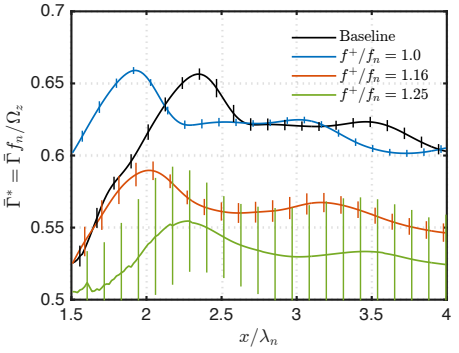

FIGURE 19. Vortex strength for cases of $\theta_0/w = 0.1$ with $f^+/f_n = 1.0$,1.16 and 1.25. In the control cases where roll-up frequency is locked onto the actuation frequency, the mean strength of the formed vortex is changed accordingly. With greater variation in the strength of each vortex, the enhanced spreading of the shear layer is also observed.

start to grow immediately behind the trailing edge at $x/\lambda_n = 0$, and their growth rates are well predicted by the local stability analysis, as shown in Figure 18 (right). When the forcing frequency departs farther from f_n, the growth rate decreases as observed for $x/\lambda_n \leqslant 2$. This can be attributed to the instability characteristics of the shear layer. When the forcing frequency is closer to f_n, the frequency with the highest spatial growth rate for the perturbation, the forcing effort grows faster since the growth rate is approaching its maximum.

The frequency spectra of the three forced cases all have distinct peaks at the forcing frequency initially for $x/\lambda_n \leqslant 3$. As $x/\lambda_n > 3$, lower frequency modes start to grow and the momentum thickness increases accordingly in Figure 18 (left). With higher f^+, the modal amplitude at the corresponding forcing frequency also decays spatially earlier in $5 \leqslant x/\lambda_n \leqslant 7$. Earlier decay of the modal amplitude at the forcing frequency also coincides with to the earlier growth of lower frequency modes in the full spectra in Figure 17 (right). Especially for the case of $f^+/f_n = 1.25$, lower frequency modes start to develop farther upstream compared to the baseline flow, resulting in a faster second growth of θ/θ_0.

In the isolated vortex region for the forced cases, thinner θ is observed when using higher f^+. This can be explained by the weaker vortex strength considering that the total vorticity flux is introduced from the inlet boundary at the same rate. With these compact vortices convecting at the mean shear layer velocity, the higher vortex passage frequency leads to lower amount of vorticity being possessed by the individual vortices, which can be confirmed from Figure 19. For the cases with $f^+/f_n = 1.16$ and 1.25, the mean vortex strengths are lower than those from the baseline and $f^+/f_n = 1.0$ cases. With weaker vortices, the reduced mixing of momentum from two streams leads to the thinner momentum thickness in the isolated vortex region. Also, the strength variations in cases of $f^+/f_n = 1.16$ and 1.25 are greater than that of the baseline. This again leads to a faster shear layer spreading than the baseline, similar to the low frequency forced cases. With $f^+/f_n = 1.0$, on the other hand, the smaller variation in vortex strength leads to a more stable isolated vortex region, leading to the wider streamwise extent than that of the baseline as shown in Figure 18 (left).

For cases with $\theta_0/w = 0.05$, the lock-on of shear layer roll-up frequency and extended isolated vortex region are still observed when forcing is invoked with $f^+/f_n = 1.00$, 1.16 and 1.25, as shown in Figure 16 and 20. However, we also note that for $\theta_0/w = 0.25$

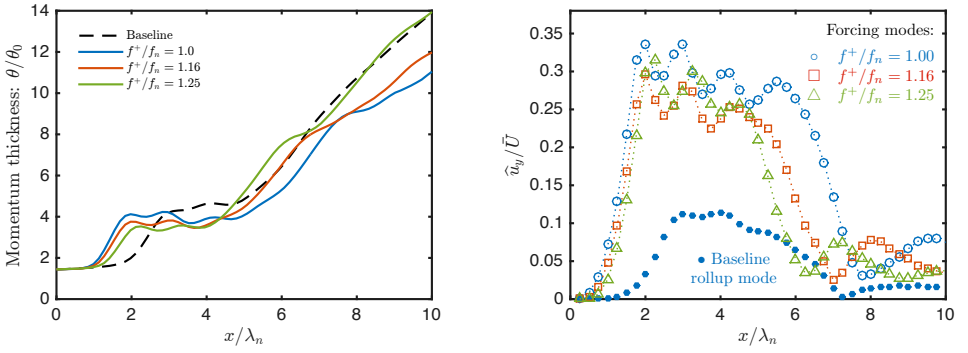

FIGURE 20. Momentum thickness growth (left) and modal amplitude growth (right) with high-frequency forcing for the $\theta_0/w = 0.05$ cases. The accelerated roll-up and amplitude growth in the forcing mode are observed to be in qualitative agreement with cases of $\theta_0/w = 0.1$.

cases, no significant changes can be seen in the shear layer for $f^+/f_n = 1.00$, 1.16, even when using a forcing amplitude of $E^+ = 0.724$, four times of the value considered earlier in this section.

3.5.3. *Roll-up delay (positive-mean heating)*

In this section, forcing effects in the shear layer from using $\dot{q}^p$ (Equation 3.2) is investigated. This form of forcing, $\dot{q}^p$, is composed of a positive DC offset added to the oscillatory $\dot{q}$. The positive DC offset introduces net positive heat transfer from the actuator and raises the mean temperature of the fluid adjacent to the actuator. With the temperature-varying viscosity model discussed in appendix 2.1, this locally increased temperature leads to a higher viscosity.

We consider representative forced cases with $E^+ = 0.741$. The effects of the locally increased viscosity is shown in Figure 21 (left). Comparing the cases with $f^+/f_n = 0$ (i.e., constant heating) and 0.500 to the baseline, the shear layer roll-up is delayed due to the locally increased viscosity. The delayed shear layer roll-up leads to an elongated recirculation region behind the trailing edge and introduces a stronger wake effect. As a consequence, the roll-up is observed to be less synchronized, as depicted in Figure 21 (right) by the less prominent peak in the roll-up mode in the spectra of the DC heating and $f^+/f_n = 0.500$ cases. The growth in the roll-up mode is also observed to reach a lower maximum amplitude than it does in the baseline flow, as show in Figure 22 (right). With the stronger wake effect and the less synchronized roll-up, the vortex strength exhibits greater variation, as shown in Figure 23. By the same mechanism discussed in the previous sections, the higher variation leads to the early deviations of the trajectories from the centerline, as well as the early merging of the vortices. Both of these effects cause the shear layer to spread faster downstream in the cases with DC heating and $f^+/f_n = 0.500$. The delayed roll-up and accelerated spreading can also be observed in the growth of θ/θ_0 from Figure 22 (left). With the subharmonic forcing added, the $f^+/f_n = 0.500$ case exhibits a greater growth in θ compared to the DC heating case. In the case with $f^+/f_n = 1.16$, the oscillatory component of $\dot{q}^p$ dominates over the DC component and still accelerates the shear layer roll-up. The changes in the vortex trajectories (Figure 21 (left)), vortex strength (Figure 23), θ/θ_0 growth (Figure 22 (left)) and the forcing mode growth (Figure 22 (right)) show similar traits to those observed in the case using $\dot{q}$ with $f^+/f_n = 1.16$.

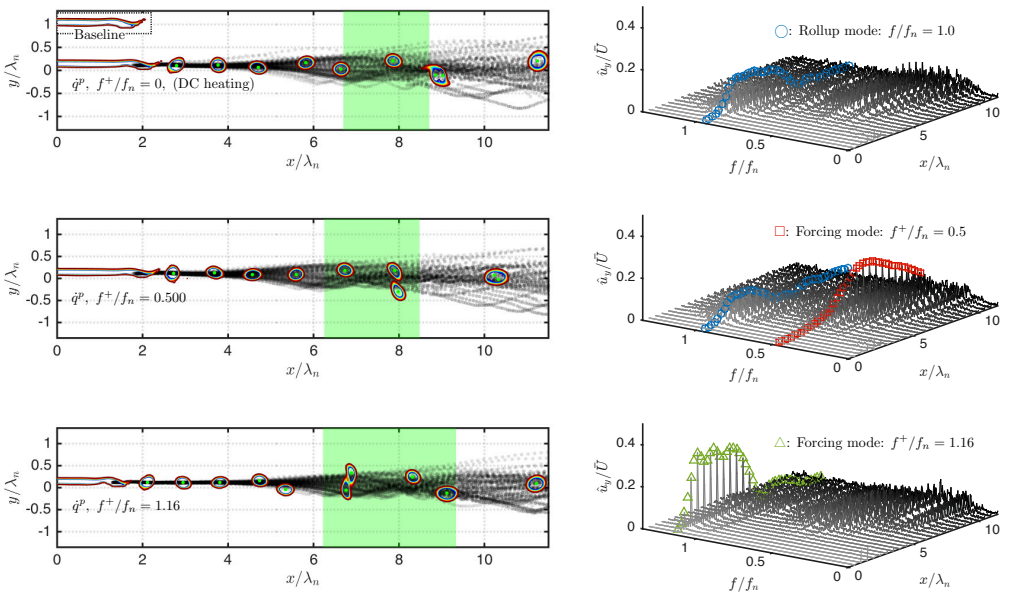

FIGURE 21. Vortex trajectories (left) and modal amplitude growth (right) for $\theta_0/w = 0.1$ cases. The merging location and its spatial variation is depicted by the green-shaded region (left) in each case.

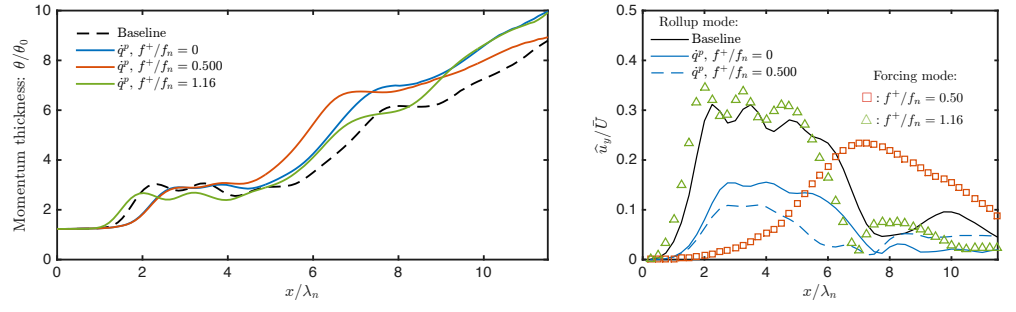

FIGURE 22. Momentum thickness growth (left) and modal amplitude growth (right) for low-frequency forcing ($\theta_0/w = 0.1$).

In the subharmonic forced case with $\dot{q}^p$, the accelerated merging built upon the delayed roll-up draws additional interests. Motivated by the observation, for cases of DC heating and $f^+/f_n = 0.500$, we further examine the effects of the forcing amplitude, E^+, in the growth of θ, as shown in Figure 24. We observe that the shear layer roll-up location, suggested by the first growth in θ, is delayed farther downstream with increased E^+, in both DC heating and subharmonic forced cases. Meanwhile, the acceleration in the spreading (second growth of θ) is also enhanced by the subharmonic forcing with increasing E^+.

Comparing the forcing effects of $\dot{q}$ and $\dot{q}^p$, we observe that the oscillatory components from both type impose similar forcing effects to the shear layer. The positive DC

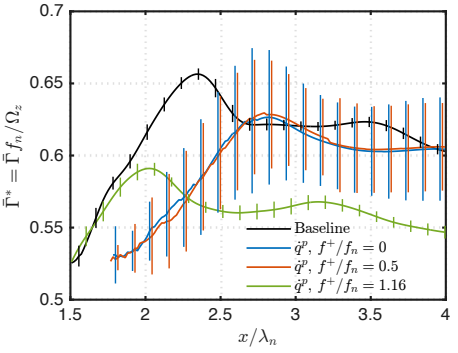

FIGURE 23. Vortex strength for cases of $\theta_0/w = 0.1$. In the cases with roll-up delay, the vortex strength is observed to have greater variation and encourage the shear layer spreading downstream. All cases are of $\theta_0/w = 0.1$.

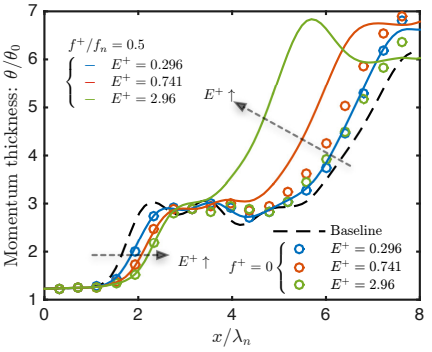

FIGURE 24. Effects of forcing amplitude (E^+) in the DC heating and subharmonic forced cases with $\dot{q}^p$. All cases are of $\theta_0/w = 0.1$.

component in $\dot{q}^p$ is able to delay the shear layer roll-up when it is not excited by the oscillatory component.

3.6. *Summary*

We numerically examined the effectiveness of local periodic heating for modifying a spatially developing shear layer downstream of a splitter plate. The early evolution of the baseline shear layer is characterized by three regions; namely, the region where vortices rolls up, the second region where vortices advect along the centerline, and the third region where vortices deviate from the centerline, leading to the merging process. The periodic heating from the trailing edge introduces a thermal perturbation to the fluid adjacent to the actuator, and consequently generates oscillatory vorticity flux over its surface and baroclinic torque in its vicinity. These added sources of vorticity perturb the strength of the vortices formed from the shear layer roll-up, and result in the change in the shear layer dynamics.

This thermal actuation technique is shown to be capable of serving as an excitation source to both the fundamental and subharmonic instabilities. When using the forcing frequency close to the first subharmonic of the shear layer roll-up frequency, the forcing can encourage vortices to deviate from the centerline and accelerate the merging process.

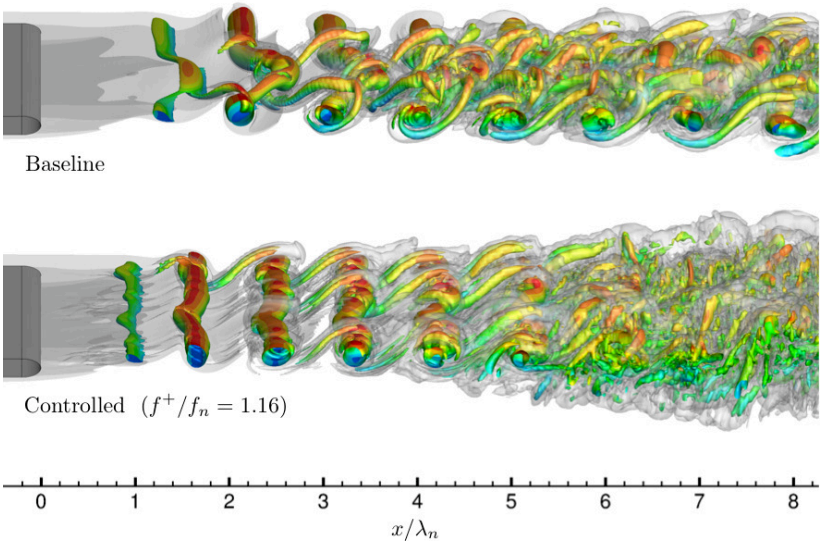

FIGURE 25. 3D LES of shear layers with $\theta_0/w = 0.1$ for the baseline and controlled cases ($f^+/f_n = 1.16$). Flow visualization uses the Q-isosurface colored by the streamwise velocity and isosurface of vorticity magnitude overlaid in transparent gray.

When the periodic heating excites the shear layer roll-up, such forcing is able to shift the roll-up frequency to the actuation frequency, and modify the mean strength of each vortex. The local momentum thickness in the isolated vortex region is also accordingly modified before further spreading takes place. The thermal actuation with positive-mean is also observed to delay the shear layer roll-up. In spite of the delayed roll-up, the subharmonic oscillatory component is still able to accelerate the downstream spreading of the shear layer. We also find that the shear layer spreading rate can be characterized by the synchronized nature of the shear layer roll-up. The lower level of roll-up synchronization correlates with the greater variance in the vortex strength, less repeatable vortex trajectories, and higher spreading rate of the shear layer.

As a final note, let us briefly mention that the same control setting is observed to be effective in modifying three-dimensional free shear layers. We perform large-eddy simulations (LES) using the same setup as in 2D simulations but extend the computational domain in the spanwise direction with the extent of $z/w = [-10, 10]$ with spanwise periodicity. Shown in Figure 25 is the instantaneous flow field, visualized using the isosurface of Q-criterion and vorticity magnitude, for the baseline and a controlled case of $\theta_0/w = 0.1$. For the controlled case, the excitation of shear layer roll-up instability is still effective in modifying the 3D shear layer with $f^+/f_n = 1.16$. Also, the enhanced shear layer spreading can also be observed in the flow visualization, as indicated by the wide transverse extent of the vortical structure in the controlled case compared to the baseline flow.

We have demonstrated that the nonlinear dynamics of a spatially developing shear layer can be modified by local oscillatory heat flux as a control input. From 3D LES, it is also shown that the local thermal forcing exhibits promising capabilities in modifying the development of turbulent shear layers downstream. In the next section, we conduct

further investigation on the use of local thermal forcing in turbulent separated flow over a canonical airfoil to explore applicational potential of present thermal actuation technique.

4. Thermal-energy-based separation control on a NACA 0012 airfoil

In the previous section, we have demonstrated that the local thermal forcing is able to excite instabilities of free shear layer and change its downstream development. This capability of modifying free shear-layer physics exhibits promising potential in the usage of thermal actuator for controlling of shear flows. In this section, we examine the effectiveness of thermal actuation for a practical scenario of aerodynamic applications: suppression of flow separation over an airfoil.

4.1. *Introduction*

Control of boundary layer separation over an airfoil has been an area of focus for the flow control community. Perturbations for active flow control can be introduced by various types of actuators (Cattafesta & Sheplak 2011), such as steady blowing/suction (Lachmann 2014), synthetic jets (Glezer & Amitay 2002), dielectric barrier discharge (DBD) plasma actuators (Corke *et al.* 2010), or combustion powered actuators (Crittenden & Raghu 2009). In most of these applications, the perturbations are introduced to the flow as a combination of mass, momentum, vorticity (i.e. angular momentum) and energy fluxes in either a steady or unsteady fashion (Joslin & Miller 2009). The weight and size of the actuators that introduce these forcing inputs as well as the amount of power required to deliver the control effort into the flow field are two main issues that often restrict the implementation of active flow control on full scale engineering systems.

Forcing efforts for active flow control can also be introduced in the form of thermal energy flux. For example, thermoacoustic actuation modeled by periodic heat flux has been examined for its effectiveness modifying the flow over a wall-mounted hump (Yeh *et al.* 2015). Thermoacoustic actuator adopts the principle of sound generation that discovered by Arnold & Crandall. (1917). They found a periodically heated platinum membrane with alternative current application is able to emit sound waves at the heating frequency. With the use of novel materials such as graphene or carbon-nanotubes for the periodically heated membrane, the operating frequency of the thermoacoustic actuator is able to cover the range of forcing frequency for flow control applications. Another example of energy-deposition-based actuation is the use of nanosecond pulse driven dielectric barrier discharge (ns-DBD) actuators (Lehmann *et al.* 2014; Little *et al.* 2012). The control mechanism of ns-DBD plasma actuation is believed to primarily rely on thermal energy (joule-heating) transfer (Adamovich *et al.* 2012; Nudnova *et al.* 2010), in contrary to alternating current driven dielectric barrier discharge (ac-DBD) actuators that employ electrohydrodynamic effect to introduce momentum perturbation (Abe *et al.* 2008; Corke *et al.* 2010). In both thermoacoustic and ns-DBD actuations, the energy-flux-based actuators have the advantage of absence of moving parts and their sheet-like arrangement, which facilitates surface-compliant installation without occupying any internal space or adding significant weight.

Motivated by the use of thermal-energy-based actuators, the objective of the present study is to gain insights into how localized heat transfer can reattach separated flows. In this preliminary study, we perform 2D and 3D large-eddy simulations of the separated flow over a NACA 0012 airfoil at an angle-of-attack $\alpha = 6^\circ$. To employ thermal actuation, local periodic heating is introduced at the natural separation point of the baseline flow. Results for controlled flow at actuation frequencies chosen in the natural shedding

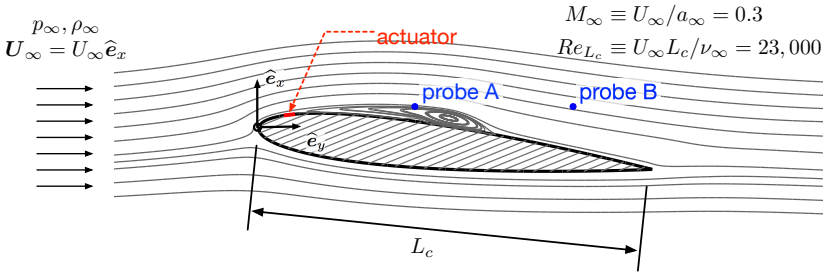

FIGURE 26. The problem description. Separated flow over a NACA 0012 airfoil at free stream Mach number of 0.3 and chord-based Reynolds number of 23,000 ($Re_{L_c} = 30,000$ for 2D LES) is used to examine its response to the forcing by local periodic heating introduced at the natural separation point.

frequency range ($St^+ \approx 0.2$) are presented. In 3D LES, the effects of spanwise actuator setup are also discussed.

4.2. *Computational setup*

4.2.1. *Problem description*

The effectiveness of using local periodic heating for control of separated flows over a NACA 0012 airfoil at an angle-of-attack $\alpha = 6^\circ$ is examined numerically. The problem setup is illustrated in Figure 26. The free stream Mach number $M_\infty \equiv U_\infty/a_\infty = 0.3$ and the chord-based Reynolds number $Re_{L_c} \equiv U_\infty L_c/\nu_\infty = 23,000$ (30,000 for 2D LES), where a_∞ and ν_∞ are the free stream sonic speed and kinematic viscosity, respectively. Thermal actuator that introduces local periodic heating is placed at the natural separation point of the baseline flow. Below, we discuss the setup for flow simulation and the boundary condition for the actuator.

4.2.2. *Computational approach*

Two- and three-dimensional large-eddy simulations for flows over a NACA 0012 airfoil at $\alpha = 6^\circ$ are performed with Vremen's sub-grid scale model. The computational domain used in this study has the domain size of $x/L_c \in [-19, 26]$, $y/L_c \in [-20, 20]$ and $z/L_c \in [-0.1, 0.1]$ for streamwise, transverse and spanwise extent, respectively, as illustrated in Figure 27. The airfoil is placed in $x/L_c \in [0, \cos\alpha]$ with its leading edge positioned at $x/L_c = y/L_c = 0$. The domain is discretized with a structured grid with a near-wall grid resolution of $\Delta y^+ = 0.3$ over the airfoil. The overall grid size is approximately 3.4×10^7 for 3D LES (3.0×10^5 for 2D).

Dirichlet boundary conditions $[\rho, p, u_x, u_y, u_z] = [\rho_\infty, p_\infty, U_\infty, 0, 0]$ are specified at the far-field computational boundary. Over the airfoil, no-slip adiabatic boundary condition is prescribed except for where the actuator is placed. The actuator model is discussed below. At the outlet boundary, non-reflective buffer zone (Freund 1997) is applied over $x/L_c \in [15, 25]$. The time integration is performed at a constant time step of $\Delta t U_\infty/L_c = 4.14 \times 10^{-5}$, corresponding to a maximum Courant-Friedrichs-Lewy (CFL) number of 0.86.

4.2.3. *Actuator model*

The thermal actuator is placed at the time-average separation point in the baseline flow, which is at $x_a/L_c = 0.083$ on the suction surface, with the size, σ, being 2% of the

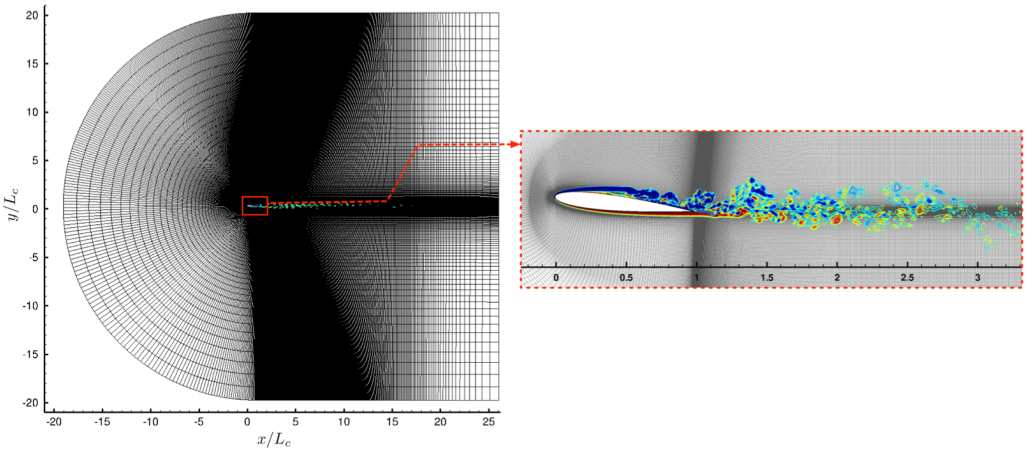

FIGURE 27. The computational domain (x-y plane). Dirichlet boundary conditions are imposed for pressure, density and velocity at the far-field. At the outflow boundary, a sponge layer is utilized for $x/L_c \geqslant 15$ to allow waves to leave the domain without numerical reflections. The near-field mesh (right) is shown with an instantaneous spanwise vorticity field from 3D LES as a reference to the mesh resolution over the airfoil and the near-wake.

chord length. The expression of the actuator model is in the form of Equation 2.5 with an additional spanwise variation for 3D simulations:

$$\dot{q} = \hat{q}\sin(2\pi f^+ t)\cos\left(\frac{\pi}{\sigma}x\right)\cos(k_z^+ z), \quad |x - x_a| \leqslant \frac{\sigma}{2}. \tag{4.1}$$

In this expression, f^+ and $\hat{q}$ are the forcing frequency and amplitude, respectively. In 3D LES, we also examine the effect of spanwise variation in heat flux by introducing the parameter k_z^+ ($k_z^+ = 0$ for 2D LES). Several choices of f^+ have been examined in their control effects on the airfoil flow based on the flow velocity spectra of the baseline flow from 2D and 3D LES, as illustrated in Figure 28, where the velocity data is collected at the probe B location shown in Figure 26. The corresponding actuation Strouhal number, $St^+ \equiv f^+(L_c \sin\alpha)/U_\infty$, ranges from $St^+ \in [0.145,\ 0.697]$ for 2D LES. Due to the computational cost for 3D LES, currently only $St^+ = 0.323$ is examined with two choices of k_z^+.

The normalized total heating power, as the expression in Equation 3.3, is

$$E^+ = \frac{f^+ \int_0^{1/f^+} \int_{|x-x_a|\leqslant\sigma/2} |\dot{q}|\mathrm{d}y\mathrm{d}t}{\frac{1}{2}\rho_\infty U_\infty^2 \cdot A U_\infty}, \tag{4.2}$$

with $A = L_c \sin\alpha$ is the frontal area of the airfoil in unit spanwise length. In the following results presented in Section 4.4, the value of the normalized actuation power is fixed at $E^+ = 0.0902$ in this study.

4.3. *Validation*

We validate 3D LES of the baseline flow over a NACA 0012 airfoil at the angle-of-attack $\alpha = 6°$ and Reynolds number $Re_{L_c} = 23,000$ by comparing the surface pressure distribution and aerodynamic forces to those reported in previous studies. Throughout this study, the pressure coefficient, C_p, lift coefficient, C_L, and drag coefficients C_D are

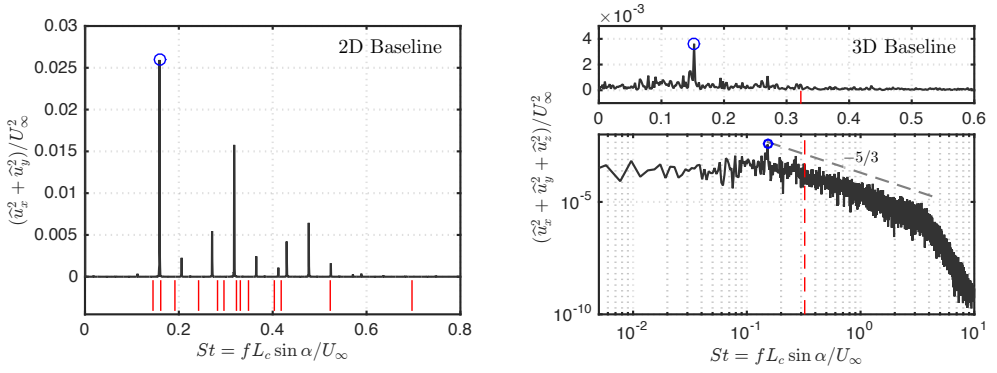

FIGURE 28. Baseline velocity spectra from at the probe B location shown in Figure 26. Left: 2D LES; Right: 3D LES. Choices of actuation frequencies, denoted with red lines, are made based on the velocity spectrum of the baseline flow. The roll-up frequency of the shear layer from the leading edge is denoted by ○. The actuation frequencies for 2D LES range from $St^+ = 0.145$ to 0.697. In 3D LES, $St^+ = 0.323$ is examined with two choices of k_z^+.

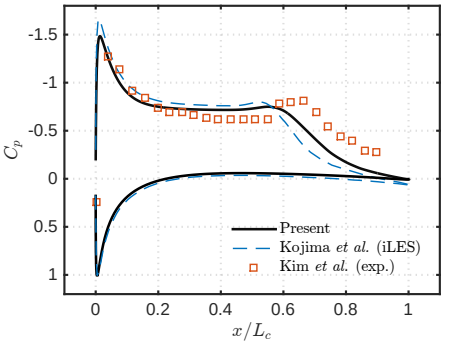

FIGURE 29. Validation of surface pressure distribution over the airfoil. Present results is compare to the numerical study by Kojima *et al.* (2013) and wind-tunnel measurement by Kim *et al.* (2009)

defined as

$$C_p = \frac{p - p_\infty}{\frac{1}{2}\rho_\infty U_\infty^2}, \quad C_L = \frac{F_L}{\frac{1}{2}\rho_\infty U_\infty^2 A}, \quad C_D = \frac{F_D}{\frac{1}{2}\rho_\infty U_\infty^2 A}, \tag{4.3}$$

where F_L and F_D are the total lift and drag force on the airfoil, respectively, and A is the planform area of the airfoil.

In Figure 29, we show the agreement in the distribution of time-average C_p over the airfoil to those reported in the numerical study with implicit large-eddy-simulation (iLES) by Kojima *et al.* (2013) and the wind-tunnel measurement by Kim *et al.* (2009) The lift and drag coefficients also exhibit reasonable agreement with the numerical studies by Kojima *et al.* (2013) and Munday & Taira (2014). With the baseline cases validated, we now proceed to investigate the control effects of local periodic heating on the separated flow over the airfoil.

Study	C_D	C_L
Present	0.065	0.619
Kojima *et al.* (2013)	0.054	0.639
Munday & Taira (2014)	0.062	0.637

TABLE 3. Coefficients of lift and drag for NACA 0012 at $\alpha = 6^\circ$ and $Re_{L_c} = 23,000$. Results show agreement with those from the numerical studies by Kojima *et al.* (2013) and Munday & Taira (2014).

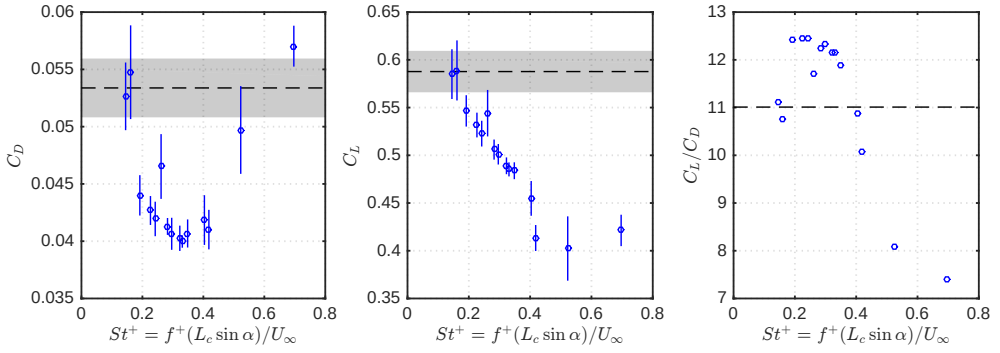

FIGURE 30. Aerodynamic forces of controlled cases compared to the baseline. The - - - - represents the time-average force of the baseline case, with the gray band characterizing the root-mean-square value of the force. The vertical bar | represent the rms value of the force from each controlled case.

4.4. *Results*

4.4.1. *2D LES*

The actuation effects of local periodic heating on the flow over the airfoil from 2D LES are discussed in this section. The simulation for baseline flow is performed for $\tau_c = tU_\infty/L_c \in [-45, 0]$ to wash out starting transients. The developed unsteady flow at $\tau_c = 0$ is then served as the initial condition for all controlled cases, which are then time-stepped to $\tau_c \approx 122$, along with the baseline flow. The flow statistics are collected in $\tau_c \in [30, 122]$ for each case.

We start our discussion by first giving an overall picture of how aerodynamic forces are changing with the actuation frequency St^+. By taking several representative cases, the discussion is continued by looking into their flow fields in detail to correlate the patterns of flow structure with the change in the time-average aerodynamic forces and their fluctuation magnitudes. The velocity profiles and surface pressure distribution for cases with enhanced and degraded aerodynamic performances are examined to reveal how they lead to the change in the aerodynamic forces on the airfoil.

As we sweep through forcing frequency, St^+, we observe change in aerodynamic forcing on the airfoil in Figure 30. In each sub-figure, the black-dashed line represents the time-average force of the baseline case, with the gray band depicting the root-mean-square (rms) value of the force. The vertical bars represent the rms values for controlled cases. We observe that, with the use of $St^+ \approx 0.2$ to 0.4, the drag is reduced noticeably. The reduction in drag saturates at $St^+ \approx 0.4$, beyond which the lift continues to decrease. Nonetheless, this trend leads to the enhanced aerodynamic performance

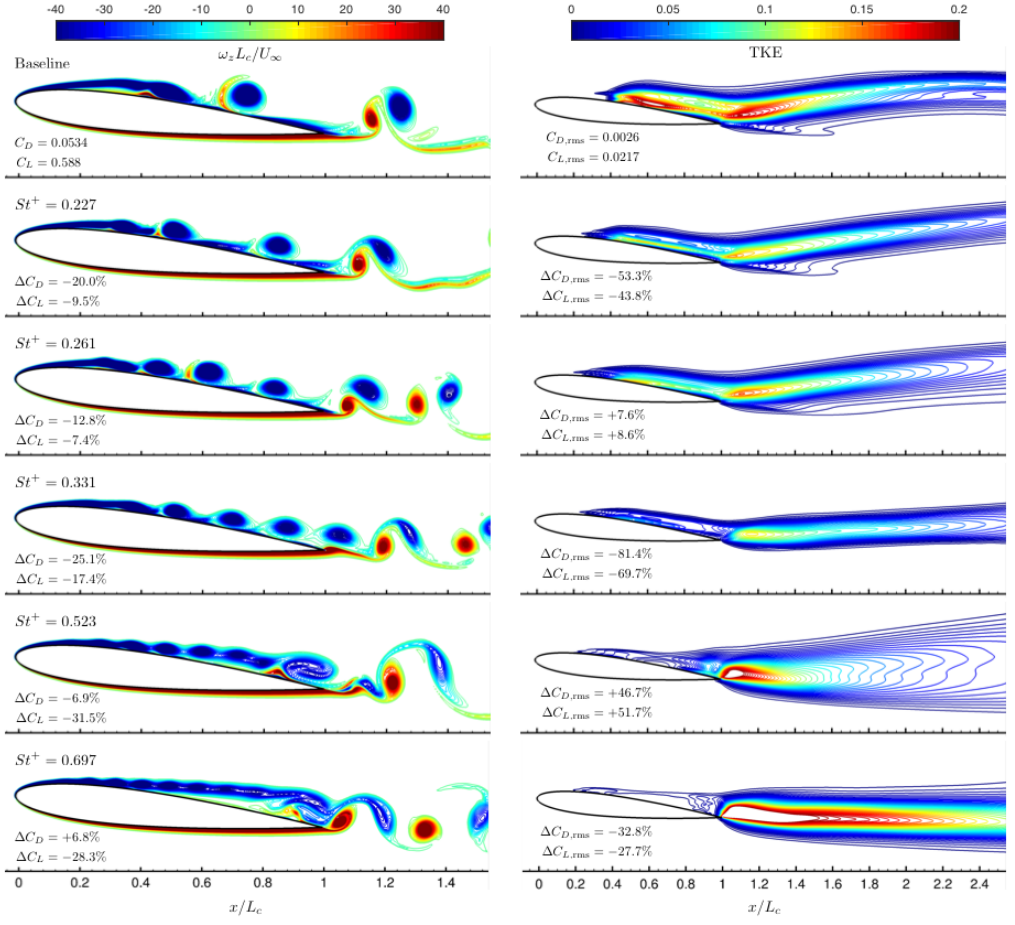

FIGURE 31. Left: The instantaneous vorticity; Right: The turbulent kinetic energy, $\mathrm{TKE} \equiv (u^2_{x,\mathrm{rms}} + u^2_{y,\mathrm{rms}})/U^2_\infty$, in the near wake. Baseline flow and five representative controlled cases are shown.

(C_L/C_D) appearing over the range of $0.2 \lessapprox St^+ \lessapprox 0.4$. All controlled cases in this range also exhibit the decrease in the magnitude of fluctuations in forces, except for $St^+ = 0.261$. For this case, we will discuss shortly while observing the flow field. We find that the use of forcing frequency of $St^+ = 0.331$ leads to the reduction in drag and its fluctuation by 25% and 81%, respectively, which are both the highest values among all controlled cases considered.

Shown in Figures 31 (left) are the instantaneous spanwise vorticity fields near the airfoil for the baseline and five representative controlled cases. It is observed that, with control, the shear layer that forms from the leading edge is attracted closer to the suction side of the airfoil, compared to that in the baseline. In all controlled cases, the shear layer carries instability wave triggered by the local periodic heating at the control frequency. This can be shown in Figure 32 (left) by the velocity spectrum collected at the probe A, as depicted in Figure 26. In this location, each controlled case has a prominent peak at the forcing frequency in the velocity spectrum. For most cases, the shear layer from the leading-edge rolls up and form compact vortices in mid-chord locations, except for the case with highest forcing frequency, $St^+ = 0.697$. This can be explained by the lower

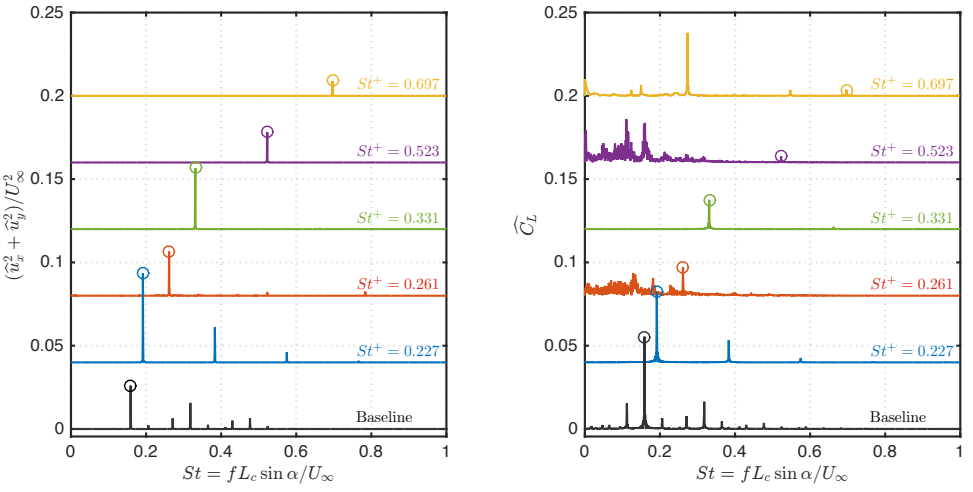

FIGURE 32. Left: frequency spectra of velocity at probe A depicted in Figure 26. The shear layer carries the instability wave at the forcing frequency depicted by ∘ with the corresponding color; right frequency spectra of lift coefficient. Baseline flow and five representative controlled cases are shown. Each spectrum is vertically shifted by 0.04 for clarity.

receptivity of the shear layer to the forcing frequency $St^+ = 0.697$. In this case, without the forming of lifting vortices (Wu *et al.* 1998) above the airfoil, we observe the largest degradation in the aerodynamic performance (C_L/C_D) with the control frequency.

It is also observed that the velocity fluctuation above the airfoil is also reduced in all controlled cases. This reduction can be seen in Figure 31 (right), with the the velocity fluctuation magnitude shown by TKE $\equiv (u^2_{x,\mathrm{rms}} + u^2_{y,\mathrm{rms}})/U^2_\infty$. Interestingly, not all controlled cases exhibit lower fluctuation in the aerodynamic forces. This can be explained by examining the far-field wake illustrated in Figure 33. The vortical structures in the wake for cases with $St^+ = 0.227$, 0.331 and 0.697 exhibit a highly repeating pattern in their spatial arrangement. However, for cases with $St^+ = 0.261$ and 0.523, where we observe higher aerodynamic force fluctuation than that in the baseline, the structures in the wake are irregular and vortex shedding is chaotic in nature. The difference in the wake pattern can also reflect the difference in frequency spectrum of the lift, as shown in Figure 32. For cases with regular wake pattern, the lift spectrum exhibits a prominent peak in either the forcing frequency or its subharmonics. But with $St^+ = 0.261$ and 0.523, the spectrum contains energetic frequency components across a broad low frequency range. This suggests that the overall vortex shedding from both side of the airfoil is not locked onto the forcing frequency, which leads to the irregular wake pattern with the use of these two control frequencies. Even though all forcing frequencies are able to introduce instability waves to the shear layer developing from the leading-edge, some frequencies, such as $St^+ = 0.261$ and 0.523 for examples, are not receptive to the other shear layer forming from the trailing-edge. As consequences, the case with $St^+ = 0.261$ behaves as an outlier in the C_L/C_D plot in Figure 30, compared to its neighboring forcing frequencies, and forcing with $St^+ = 0.523$ results in the highest reduction in lift and highest increase in the aerodynamic force fluctuations.

Next, we choose two representative controlled cases and the baseline to discuss the

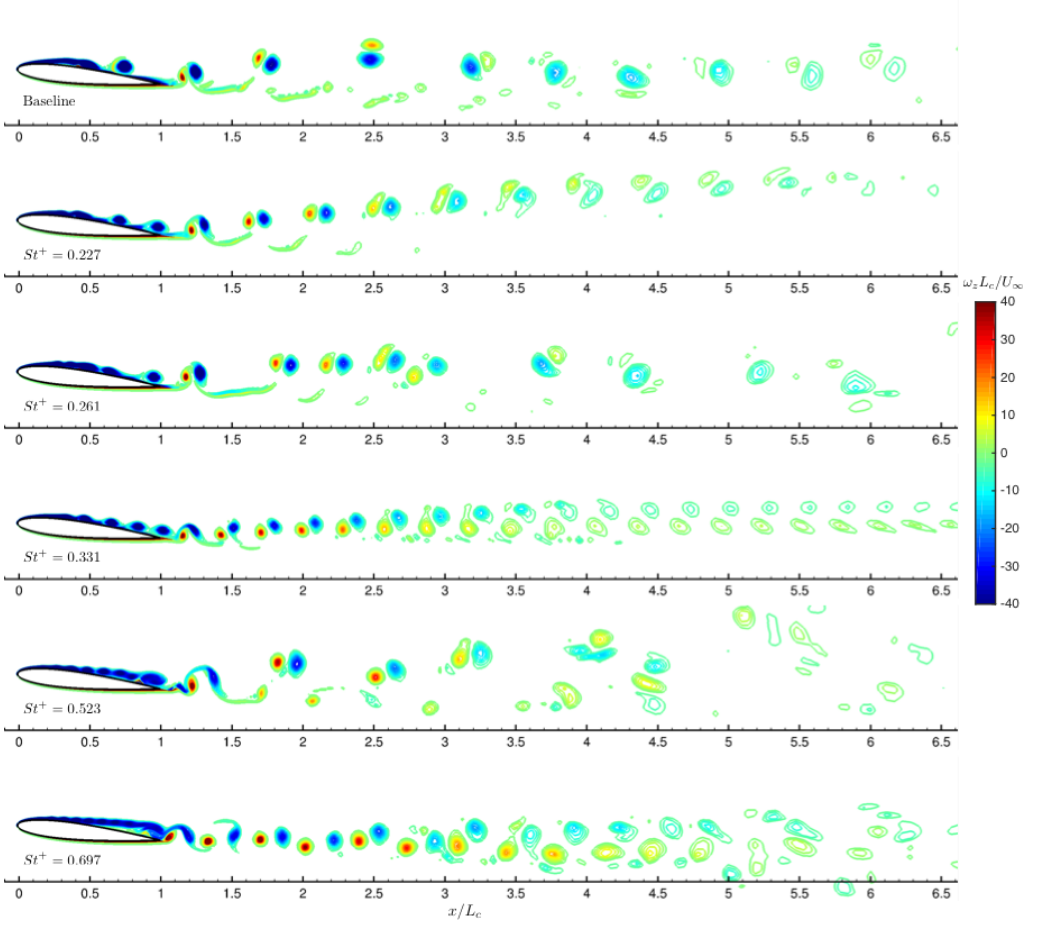

FIGURE 33. Instantaneous vorticity field of the far-field wake. Baseline flow and five representative controlled cases are shown.

change in the time-average velocity profile over the airfoil and the distribution of surface pressure. Two controlled cases chosen here are:

(i) $St^+ = 0.331$, the case with the largest reduction in drag and force fluctuations;

(ii) $St^+ = 0.523$, the case with highest reduction in lift and most increase in the force fluctuations.

Figure 34 shows the time-average streamwise velocity profiles at streamwise stations of $x/L_c = 0.05$ to 0.85 and the zero-streamwise-velocity contour lines, which are used to characterize the extent of the recirculation bubble for each case. For stations behind the location of the actuator, $x/L_c = 0.083$, the streamwise velocity profiles exhibit a fuller shape (i.e., smaller velocity deficit from U_∞) compared to the baseline. Also, $(\mathrm{d}\bar{u}/\mathrm{d}y)_w > 0$ is recovered at $x/L_c \approx 0.45$, farther upstream than the baseline. This suggests that the separated boundary layer from the leading-edge reattaches to the suction surface of the airfoil at a upstream location comparing to the baseline flow, which leads to a smaller streamwise extent of recirculation region in both controlled cases with $St^+ = 0.331$ and 0.523. However, for the controlled case with $St^+ = 0.523$, the flow separates again at $x/L_c \approx 0.5$. This second separation is clearly seen from the $\overline{u}_x = 0$ contour lines for the $St^+ = 0.523$ case. A large recirculation bubble appears in $x/L_c > 0.5$ for this case

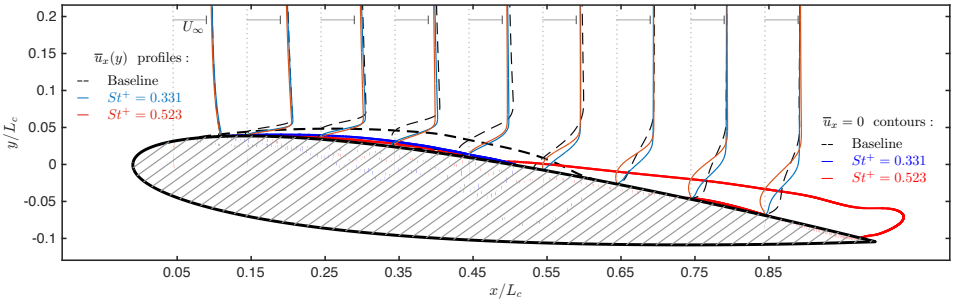

FIGURE 34. The time-average streamwise velocity profiles at streamwise stations of $x/L_c \in [0.05, 0.85]$ and zero-streamwise-velocity contours above the airfoil. Both suggest the change in size of the recirculation bubble.

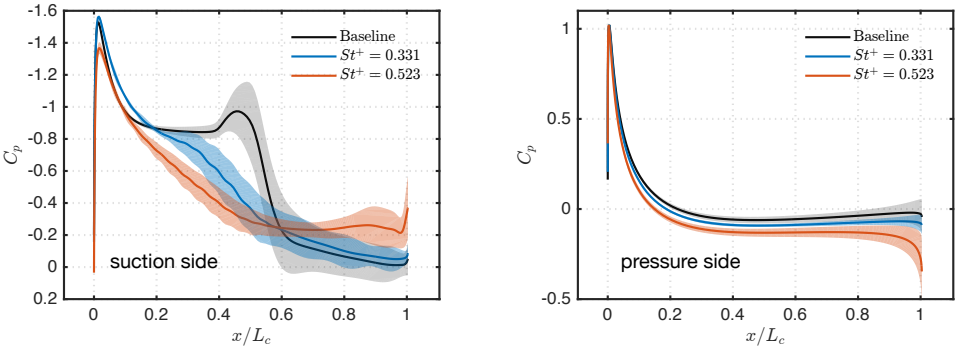

FIGURE 35. Coefficent of pressure, $C_p = (p - p_\infty)/\frac{1}{2}\rho_\infty U_\infty^2$, over the suction surface (left) and pressure surface (right) of the airfoil. The color band denotes $C_{p,\mathrm{rms}}$, the local root-mean-square value of C_p.

and leads to the degradation in the aerodynamic performance. The formation of this recirculation bubble can be attributed to the positive vorticity leakage from the pressure side, as shown in Figure 31 (left) in the $St^+ = 0.523$ case.

With the same controlled cases, we show the change in the distribution of surface pressure and its fluctuation magnitude. Illustrated in Figure 35, is the time-average C_p for each case, with the corresponding color band characterizing the local pressure fluctuation. For case with $St^+ = 0.331$, pressure distribution shows a higher suction in $x/L_c \lesssim 0.2$ and a lower suction in $0.2 \lesssim x/L_c \lesssim 0.6$, as shown in the left for the suction side of the airfoil. A greater decease in suction is observe for the $St^+ = 0.523$ case in $0.2 \lesssim x/L_c \lesssim 0.6$. For this case, the pressure fluctuation is also observed to be higher in the region near the trailing-edge. This can be also seen from the velocity fluctuation in Figure 31 (right). The velocity fluctuation near the trailing-edge is also found to be greater than that of the baseline case. On the pressure side, both controlled cases show a lower pressure distribution than the baseline. The change in the surface pressure distribution results in the decrease in both lift and drag, but for case with $St^+ = 0.331$ this leads to an aerodynamically favorable change in the increase of C_L/C_D by 10% with lower force fluctuations.

Let us briefly summarize our 2D findings. From the results of 2D LES, we observe that the control effect of local periodic heating is sensitive to the forcing frequency. To

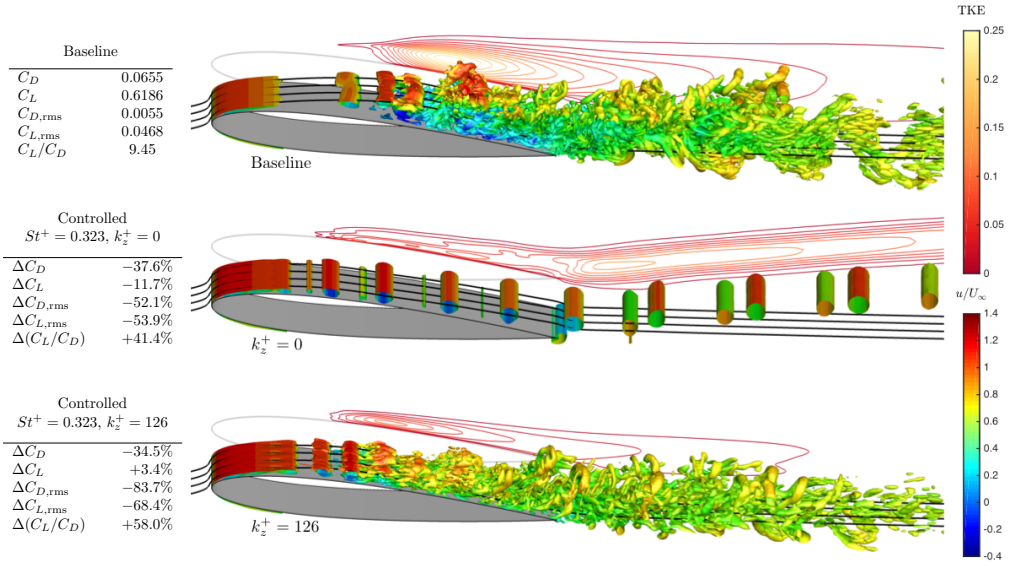

FIGURE 36. Instantaneous flow fields for baseline and two controlled cases with $k_z^+ = 0$ and 126 and $St^+ = 0.323$. Visualization of flow structure with Q-criterion iso-surface colored with streamwise velocity. Time-average streamlines above the airfoil are shown. The velocity fluctuation magnitude is also illustrated behind the instantaneous flow field for each case. The changes in the aerodynamic forces and their fluctuation magnitudes are tabulated on the left.

achieve aerodynamically favorable control, both shear layers from the leading-edge and the trailing-edge need to be receptive to the forcing frequency. With appropriate control settings, we observe the lock-on of vortex shedding to the actuation frequency and an ordered pattern in the spatial arrangement for the vortical structures in the wake. The enhancement in aerodynamic performance generally correlates with the decrease in the fluctuations of the aerodynamic forces. Leveraging the knowledge gained from 2D LES, we proceed our investigation on control effect in three-dimensional setups.

4.4.2. *3D LES*

Due to the computational cost for 3D LES, we present two controlled cases with the same actuation frequency, $St^+ = 0.323$, but different spanwise actuator setup in the choice of $k_z^+ = 0$ and 126. For the latter case, it corresponds to $\lambda_z^+ = 0.05L_c$, where λ_z^+ is the forcing wave length in spanwise direction. Using a instantaneous flow field of the 2D baseline flow as the initial condition, we perform 3D LES for the baseline flow for $\tau_c = tU_\infty/L_c \in [-30, 0]$ to allow for full development of 3D structures. The developed 3D flow at $\tau_c = 0$ is then served as the initial condition for all controlled cases, which are then time-stepped to $\tau_c \approx 60$, along with the baseline flow simulation. The flow statistics are collected in $\tau_c \in [10, 60]$ for each case. In the 3D baseline case, the laminar boundary layer separates at $x/L_c \approx 0.1$ and forms a 2D shear layer. The shear layer rolls up at $x/L_c \approx 0.4$ and develops into fully 3D turbulent structure for $x/L_c > 0.5$ in the recirculation bubble, as shown in Figure 36 (top).

We start our discussions on the controlled flow with the case with $k_z^+ = 0$. In this case, we find the actuation is able to excite the fundamental roll-up of the shear layer, which in turn laminarizes the separated flow and diminishes the development of 3D

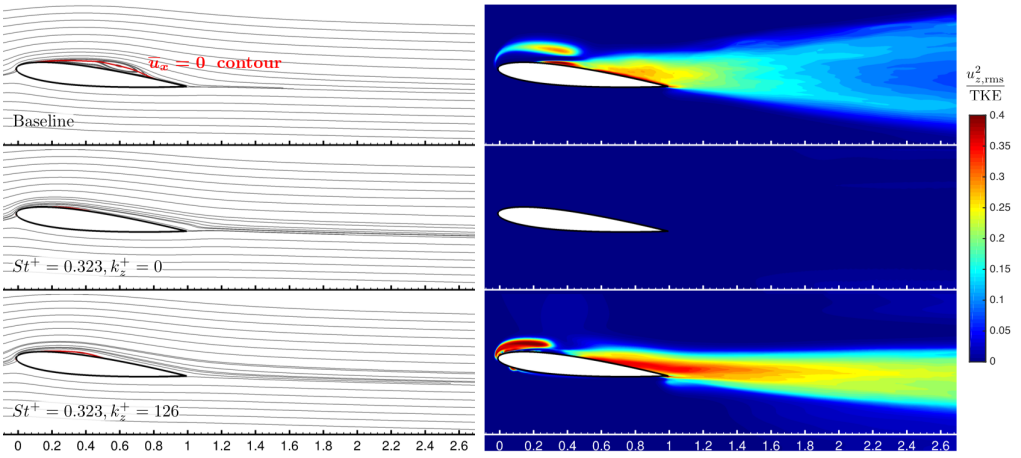

FIGURE 37. Left: the time-average streamlines and the zero streamwise velocity contour; Right: the locally normalized spanwise velocity fluctuation, namely $u^2_{z,\mathrm{rms}}/\mathrm{TKE}$, where $\mathrm{TKE} \equiv (u^2_{x,\mathrm{rms}} + u^2_{y,\mathrm{rms}} + u^2_{z,\mathrm{rms}})$

structures. As shown in Figure 36 (middle), forcing inputs with $k_z^+ = 0$ chops the shear layer at the forcing frequency. Each chop forms a compact 2D vortical structures that advect closely along the suction side of the airfoil, leading to the surface conforming streamlines above the airfoil. In Figure 37 (left), we characterize the recirculation region by the contour line of zero time- and spanwise-average streamwise velocity. Compared to the baseline, we observe that the recirculation bubble is nearly diminished in size and the flow is attached over the suction surface. In Figure 37 (right), we show the locally normalized spanwise velocity fluctuation, namely $u^2_{z,\mathrm{rms}}/(u^2_{x,\mathrm{rms}} + u^2_{y,\mathrm{rms}} + u^2_{z,\mathrm{rms}})$. The quiet spanwise fluctuation field in Figure 37 (right-middle) also agrees with the flow structures we observe in Figure 36 (middle), where only spanwise vortical structures are observed in the case with $k_z^+ = 0$.

The three-dimensional instability characteristics for a 2D shear layer have been theoretically studied by Pierrehumbert & Widnall (1982). Their study shows that a 2D shear layer is most receptive to perturbations without spanwise variations ($k_z = 0$). With the highest growth rate in 2D perturbations, the 2D control repetitively produces vortical structures without spanwise variation and traps energy of perturbation in the 2D coherent structures. The 2D vortex shedding from both suction and pressure side of the airfoil is locked onto the forcing frequency, which can be seen in both frequency spectrum for velocity and lift coefficient in Figure 38 by the prominent peak at the forcing frequency. In the study on the thermal forcing input with $k_z^+ = 0$ in 3D LES, we observe the drag reduction of 37.6%, even higher than that in the 2D LES study. The aerodynamic performance C_L/C_D is also increased by 41.4% with control.

We also introduce a spanwise variation in the actuator setup by using $k_z^+ = 126$. This spanwise setup is resolved by 32 grid points per wave. In this case, we found the excited the roll-up structure carries the spanwise perturbation introduced from the actuator, as shown in Figure 36 (bottom) near the leading-edge. The shear layer roll-up is locked onto the first harmonic of the forcing frequency, as opposed to that with 2D control. Leveraging the spanwise instability, these structures evolve with higher level of three-dimensional mixing, compared to the baseline case. This higher spanwise fluctuation

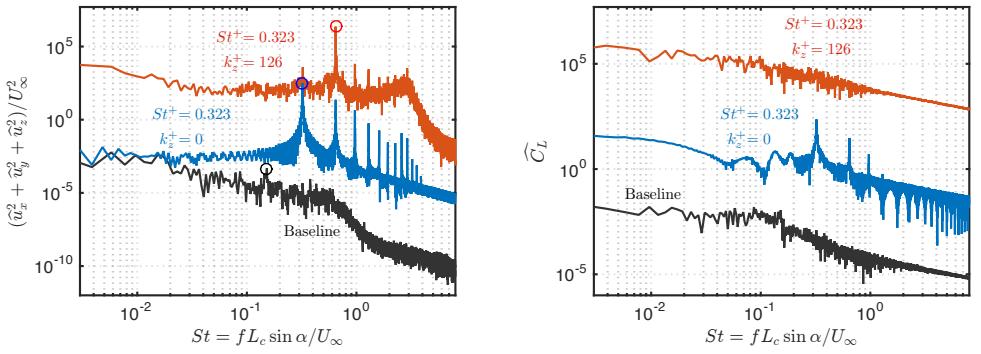

FIGURE 38. Frequency spectra for 3D LES. Left: frequency spectra of velocity at probe A depicted in Figure 26. The peak at the roll-up frequency of the shear layer is depicted by ∘ with the corresponding color; Right: frequency spectra of lift coefficient. Baseline flow and controlled cases are shown. Each spectrum is vertically shifted by 4 decades for clarity.

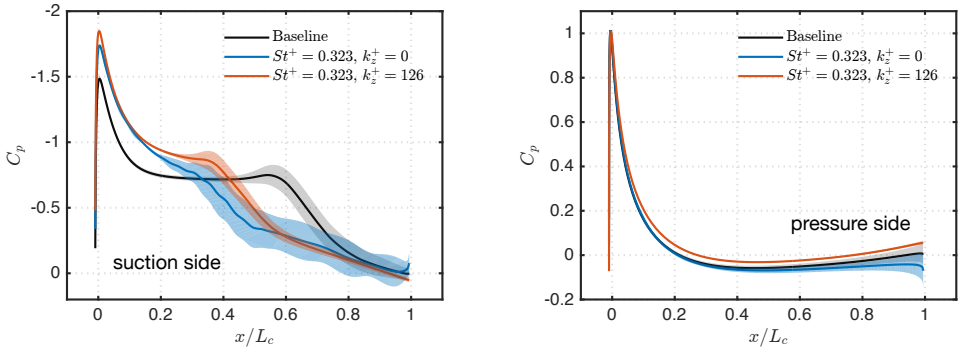

FIGURE 39. Coefficent of pressure C_p over the suction surface (left) and pressure surface (right) of the airfoil. The color bands denotes $C_{p,\mathrm{rms}}$, the local root-mean-square value of C_p.

with 3D control can be seen in Figure 37 (right-bottom). These structures with higher 3D mixing advect towards the trailing-edge of the airfoil and merges with the stream from the pressure side. This merging forms another shear layer that carries spanwise fluctuation of comparable magnitude to those in the other two directions. As pointed out by Pierrehumbert & Widnall (1982), the spanwise fluctuation can result in a more stable shear layer to streamwise perturbations. As a consequence, control with $k_z^+ = 126$ suppresses the emergence of the large 2D von Kármán vortical structures in the wake, which are observed to be prominent in the baseline flow. In the case with $k_z^+ = 126$, the surface pressure shown in Figure 39 also exhibits much lower level of fluctuation on both side of the airfoil. Moreover, this controlled case shows a higher suction in $x \leqslant 0.4$ on the suction side and also a higher pressure over the whole chord length on the pressure side, compared to the baseline. The change in suction and pressure leads to an increase in lift by 3.4% and the drag reduction by 34.5%, resulting in the increase of C_L/C_D by 58% compared to the baseline. The fluctuations in aerodynamic forces are also reduce by up to 83% with 3D control.

4.5. *Summary*

The effectiveness of the use of local periodic heating for flow control on the separated flow over NACA 0012 airfoil at $\alpha = 6^\circ$ is numerically examined. In 2D LES, the results show the thermal control technique is able to reattach the flow earlier upstream with the use of the forcing frequency $St^+ \in [0.2, 0.4]$. With the forcing frequency that excites both lead- and trailing-edge shear layer instabilities, we observe the drag on the airfoil is reduced by up to 24.4% accompanied by a small decrease in lift. The overall aerodynamic performance can be enhanced by up to 13.2%. The fluctuations in aerodynamic forces is also reduced by up to 81.4%. In 3D LES with $k_z^+ = 0$, we find the actuation is able to excite the fundamental roll-up of the shear layer, which in turn laminarizes the separated flow and diminishes the development of 3D structures. The control with $k_z^+ = 0$ repetitively produces vortical structures without spanwise variation and traps the perturbation energy in the 2D coherent structures. This 2D vortex shedding from both suction and pressure side of the airfoil is locked onto the forcing frequency. In the controlled case with $k_z^+ = 126$, we found the excited the roll-up structure carries the spanwise perturbation introduced from the actuator. Leveraging the spanwise instability, these structures evolve with higher level of three-dimensional mixing while advecting towards the trailing edge of the airfoil, and suppresses the emergence of large 2D von Kármán type vortical structures in the wake, which are observed to be prominent in the baseline flow. The lift is increased by 3.4% and the drag is reduced by 34.5%, resulting in the increase of C_L/C_D by 58%. The fluctuations in aerodynamic forces are also reduce by up to 83% with $k_z^+ = 126$.

We have shown that the forcing with local periodic heating can effectively modify the separated flow over the airfoil in an aerodynamically favorable manner. We also discuss the advantage of the benefits of this thermal-energy-based flow control technique compared to other mass- and momentum-based flow actuation. In this fluid flow problem of separated flow over an airfoil, the thermal-based actuator has demonstrated great potential of reattaching the flow and enhancing the aerodynamic performance. Thus, we propose to pursue further study on the use of thermal-based actuation for flow control over a NACA 0012 airfoil by expanding the choices of forcing frequency St^+ and the forcing wavenumber k_z^+ supported with companion instability analyses. The detailed further work will be discussed in the following section.

5. Concluding remarks

5.1. *Conclusion*

We have demonstrated that the use of fundamental thermal actuation can effectively modify nonlinear dynamics in both fluid flows of interest. In Section 3, we started with a fundamental investigation on a free shear layer perturbed by a local periodic heating. We found that the oscillatory thermal forcing translates to hydrodynamic perturbation in the form of oscillatory surface vorticity flux and baroclinic torque at the actuation frequency in the vicinity of the trailing edge. The produced vortical perturbations can independently excite the fundamental instability that accounts for shear layer roll-up as well as the subharmonic instability that encourages the vortex pairing process farther downstream. The time-average momentum profiles are also correspondingly changed by the modification in these aforementioned nonlinear phenomena in the free shear layer. In Section 4, we examine the use of thermal actuation on the separated flow over a NACA 0012 airfoil at 6° angle-of-attack and chord-based Reynolds number $Re_{L_c} = 23,000$. We observe that the unsteady thermal forcing is capable of suppressing the flow separation

from leading edge by triggering the roll-up of the shear layer. In 3D LES, we observe setup with a spanwise strip for the actuator is able to laminarize the flow by repetitively producing spanwise vortical structures and traps the perturbation energy in the 2D coherent structures. When a spanwise variation is introduced to the thermal actuation, we observe that the forcing can enhance the 3D mixing over the airfoil and the entrainment of free-stream momentum. The drag is significantly reduced by up to 35% accompanied by a 3.4% lift increase. The fluctuations in the aerodynamic forces are also reduced by up to 84%. With the research efforts up to date, we believe that they have provided understanding of the control mechanism with thermal-based actuation and provided a possible pathway towards flow control using actuators such as thermophones and pulse driven plasma actuators.

At the moment, we are still investigating additional forcing frequencies and spanwise wavenumbers for the thermal actuation on flow over the airfoil. Actuation effect at a higher angle-of-attack, $\alpha = 9°$, will also be examined. Moreover, we propose to perform instability analyses using two different approaches in order to provide guidance to physics-based design of active flow control using thermal-based actuators.

5.2. *Acknowledgements*

We thank the support from the US Army Research Office that made this research possible. We also are grateful to the computational time made available by the High Performance Computing Modernization Program at the Department of Defense.

5.3. *Resulting publications*

The papers produced from this research effort to date are listed below:

- Yeh, C.-A., Munday, P. M., Taira K. and Munson, M. J. 2015 *Drag Reduction Control for Flow over a Hump with Surface-Mounted Thermoacoustic Actuator*, AIAA paper 2015-0826 (See: Yeh *et al.* 2015).
- Yeh, C.-A., Munday, P. M. and Taira, K. 2017, *Laminar Shear Layer Modification Using Localized Periodic Heating*, Journal of Fluid Mechanics (See: Yeh *et al.* 2017*a*).
- Yeh, C.-A., Munday, P. M. and Taira, K. 2017 *Use of Local Periodic Heating for Separation Control on a NACA 0012 Airfoil*, AIAA paper 2017-1451 (See: Yeh *et al.* 2017*b*).
- Yeh, C.-A., Sun, Y. and Taira, K. 2017 *Thermal-Based Separation Control of Flow over an Airfoil and its Resolvent Analysis*, 9th JSME-KSME Thermal and Fluids Engineering Conference, Okinawa, October 28-30, 2017 (See: Yeh *et al.* 2017*c*).

REFERENCES

Abe, T., Takizawa, Y., Sato, S. & Kimura, N. 2008 Experimental study for momentum transfer in a dielectric barrier discharge plasma actuator. *AIAA Journal* **46** (9), 2248–2256.

Adamovich, I. V., Leonov, S. B., Frederickson, K., Zheng, J., Cui, Y. & Khoo, B. C. 2017 Thermal perturbations generated by near-surface electric discharges and mechanisms of their interaction with the airflow. In *55th AIAA Aerospace Sciences Meeting*, p. 1339.

Adamovich, I. V., Little, J., Nishihara, M., Takashima, K. & Samimy, M. 2012 Nanosecond pulse surface discharges for high-speed flow control. In *AIAA Paper 2012-3137*.

Akins, D., Singh, A. & Little, J. 2015 Effects of pulse energy on shear layer control using surface plasma discharges. In *AIAA Paper 2015-3344*.

Aleksandrov, N. L., Kindysheva, S. V., Nudnova, M. M. & Starikovskiy, A. Yu 2010

Mechanism of ultra-fast heating in a non-equilibrium weakly ionized air discharge plasma in high electric fields. *Journal of Physics D: Applied Physics* **43** (25), 255201.

Arnold, H. D. & Crandall., I. B. 1917 The thermophone as a precision source of sound. *Physical Review* **10**, 22–38.

Asrar, W. & Nayfeh, A. H. 1985 Nonparallel stability of heated two-dimensional boundary layers. *The Physics of fluids* **28** (5), 1263–1272.

Barone, M. F. & Lele, S. K. 2005 Receptivity of the compressible mixing layer. *Journal of Fluid Mechanics* **540**, 301–335.

Bechert, D. W. 1988 Excitation of instability waves in free shear layers. Part 1. Theory. *Journal of Fluid Mechanics* **186**, 47–62.

Bechert, D. W. & Stahl, B 1988 Excitation of instability waves in free shear layers. Part 2. Experiments. *Journal of Fluid Mechanics* **186**, 63–84.

Bin, Jonghoon, Oates, William S & Taira, Kunihiko 2015 Thermoacoustic modeling and uncertainty analysis of two-dimensional conductive membranes. *Journal of Applied Physics* **117** (6), 064506.

Brès, G. A., Ham, F. E., Nichols, J. W. & Lele, S. K. 2017 Unstructured large-eddy simulations of supersonic jets. *AIAA Journal* **55** (4), 1164–1184.

Brown, G. L & Roshko, A. 1974 On density effects and large structure in turbulent mixing layers. *Journal of Fluid Mechanics* **64** (04), 775–816.

Cattafesta, L. N. & Sheplak, M. 2011 Actuators for active flow control. *Annual Review of Fluid Mechanics* **43**, 247–272.

Cattafesta, L. N., Song, Q., Williams, D. R., Rowley, C. W. & Alvi, F. S. 2008 Active control of flow-induced cavity oscillations. *Progress in Aerospace Sciences* **44**, 479–502.

Cheung, L. C. & Lele, S. K. 2009 The dynamics of nonlinear instability waves in laminar heated and unheated compressible mixing layers. *Physics of Fluids* **21** (9), 094103.

Choi, H. & Moin, P. 2012 Grid-point requirements for large eddy simulation: Chapman?s estimates revisited. *Physics of Fluids* **24** (1), 011702.

Clemens, N. T. & Mungal, M. G. 1995 Large-scale structure and entrainment in the supersonic mixing layer. *Journal of Fluid Mechanics* **284**, 171–216.

Corke, T. C., Enloe, C. L. & Wilkinson, S. P. 2010 Dielectric barrier discharge plasma actuators for flow control. *Annual Review of Fluid Mechanics* **42**, 505–529.

Corke, T. C., He, C. & Patel, M. 2009 Plasma flaps and slats: an application of weakly-ionized plasma actuators. *Journal of Aircraft* **46** (3), 864–873.

Crighton, D. G. 1985 The Kutta condition in unsteady flow. *Annual Review of Fluid Mechanics* **17** (1), 411–445.

Crittenden, T. M. & Raghu, S. 2009 Combustion powered actuator with integrated high frequency oscillator. *Int. J. Flow Control* **1**, 87–97.

Elliott, G. S. & Samimy, M. 1990 Compressibility effects in free shear layers. *Physics of Fluids* **2** (7), 1231–1240.

Franck, J. A. & Colonius, T. 2010 Compressible large-eddy simulation of separation control on a wall-mounted hump. *AIAA J.* **48** (6), 1098–1107.

Freund, J. B. 1997 Proposed inflow/outflow boundary condition for direct computation of aerodynamic sound. *AIAA Journal* **35** (4), 740–742.

Garnier, E., Adams, N. & Sagaut, P. 2009 *Large eddy simulation for compressible flows*. Springer Science & Business Media.

Glezer, A. & Amitay, M. 2002 Synthetic jets. *Annual Review of Fluid Mechanics* **34** (1), 503–529.

Greenblatt, D., Paschal, K. B., Yao, C.-S. & Harris, J. 2006 Experimental investigation of separation control part 2: Zero mass-flux oscillatory blowing. *AIAA Journal* **44** (12), 2831–2845.

Gad-el Hak, M. & Bushnell, D. M. 1991 Separation control: review. *Journal of Fluids Engineering* **113** (1), 5–30.

Ho, C.-M. & Huang, L.-S. 1982 Subharmonics and vortex merging in mixing layers. *Journal of Fluid Mechanics* **119**, 443–473.

Ho, C.-M. & Huerre, P. 1984 Perturbed free shear layers. *Annual Review of Fluid Mechanics* **16** (1), 365–422.

Hornung, H. 1989 Vorticity generation and transport. In *10th Australasian fluid mechanics conference, Paper KS-3*.

Joslin, R. D. & Miller, D. N. 2009 *Fundamentals and applications of modern flow control*. American Institute of Aeronautics and Astronautics.

Khalighi, Y., Ham, F., Moin, P., Lele, S., Schlinker, R., Reba, R. & Simonich, J. 2011*a* Noise prediction of pressure-mismatched jets using unstructured large eddy simulation. Proceedings of ASME Turbo Expo, Vancouver: American Society of Mechanical Engineers.

Khalighi, Y., Nichols, J. W., Ham, F., Lele, S. K. & Moin, P. 2011*b* Unstructured large eddy simulation for prediction of noise issued from turbulent jets in various configurations. In *AIAA Paper 2011-2886*.

Kim, D.-H., Yang, J.-H., Chang, J.-W. & Chung, J. 2009 Boundary layer and near-wake measurements of NACA 0012 airfoil at low reynolds numbers.

Kojima, R., Nonomura, T., Oyama, A. & Fujii, K. 2013 Large-eddy simulation of low-reynolds-number flow over thick and thin NACA airfoils. *Journal of Aircraft* **50** (1), 187–196.

Kourta, A., Braza, M., Chassaing, P. & Haminh, H. 1987 Numerical analysis of a natural and excited two-dimensional mixing layer. *AIAA Journal* **25** (2), 279–286.

Kral, L. D. & Fasel, H. F. 1994 Direct numerical simulation of passive control of three-dimensional phenomena in boundary-layer transition using wall heating. *Journal of Fluid Mechanics* **264**, 213–254.

Lachmann, G. V. 2014 *Boundary layer and flow control: its principles and application*. Elsevier.

Laizet, S., Lardeau, S. & Lamballais, E. 2010 Direct numerical simulation of a mixing layer downstream a thick splitter plate. *Physics of Fluids* **22** (1), 015104.

Landrum, D. & Macha, J. 1987 Influence of a heated leading edge on boundary layer growth, stability, and transition. In *AIAA Paper 1987-1259*, p. 1259.

Lauchle, G. C. & Gurney, G. B. 1984 Laminar boundary-layer transition on a heated underwater body. *Journal of Fluid Mechanics* **144**, 79–101.

Lehmann, R., Akins, D. & Little, J. 2014 Effects of ns-DBD plasma actuators on turbulent shear layers. In *AIAA Paper 2014-2220*.

Linke, W 1942 Über den strömungswiderstand einer beheizten ebenen platte. *Lüftfahrt-forschung* **19**, 157–160.

Little, J., Takashima, K., Nishihara, M., Adamovich, I. V. & Samimy, M. 2012 Separation control with nanosecond-pulse-driven dielectric barrier discharge plasma actuators. *AIAA Journal* **50** (2), 350–365.

Lowell, R. L. & Reshotko, E. 1974 Numerical study of the stability of a heated boundary layer. *Tech. Rep.* TR-73-95. Case Western Reserve University Rep FTAS.

Mehta, R. D. 1991 Effect of velocity ratio on plane mixing layer development: Influence of the splitter plate wake. *Experiments in Fluids* **10** (4), 194–204.

Monkewitz, P. A. & Huerre, P. 1982 Influence of the velocity ratio on the spatial instability of mixing layers. *Physics of Fluids* **25** (7), 1137–1143.

Munday, P. M. & Taira, K. 2014 Separation control on NACA 0012 airfoil using momentum and wall-normal vorticity injection. In *AIAA Paper 2014-2685*, p. 2685.

Nudnova, M. M., Aleksandrov, N. L. & Starikovskii, A. Y. 2010 Influence of the voltage polarity on the properties of a nanosecond surface barrier discharge in atmospheric-pressure air. *Plasma Physics Reports* **36** (1), 90–98.

Papamoschou, D. & Roshko, A. 1988 The compressible turbulent shear layer: an experimental study. *Journal of Fluid Mechanics* **197**, 453–477.

Pierrehumbert, R. T. & Widnall, S. E. 1982 The two-and three-dimensional instabilities of a spatially periodic shear layer. *Journal of Fluid Mechanics* **114**, 59–82.

Popov, N. A. 2011 Fast gas heating in a nitrogen–oxygen discharge plasma: I. kinetic mechanism. *Journal of Physics D: Applied Physics* **44** (28), 285201.

Post, M. L. & Corke, T. C. 2004 Separation control on high angle of attack airfoil using plasma actuators. *AIAA Journal* **42** (11), 2177–2184.

Rathay, N., Boucher, M., Amitay, M. & Whalen, E. 2014 Parametric study of synthetic-jet-based control for performance enhancement of a vertical tail. *AIAA Journal* **52** (11), 2440–2454.

Rumsey, C. L., Gatski, T. B., III, W. L. Sellerts, Vatsa, V. N. & Viken, S. A. 2006

Summary of the 2004 computational fluid dynamics validation workshop on synthetic jets. *AIAA J.* **44** (2), 194–207.

Sabatini, R. & Bailly, C. 2014 Numerical algorithm for computing acoustic and vortical spatial instability waves. *AIAA Journal* **53** (3), 692–702.

Samimy, M., Kim, J.-H., Kastner, J., Adamovich, I. V. & Utkin, Y 2007 Active control of high-speed and high-Reynolds-number jets using plasma actuators. *Journal of Fluid Mechanics* **578**, 305–330.

Schlichting, H. 1968 Boundary-layer theory .

Seifert, A. & Pack, L. G. 1999 Oscillatory control of separation at high Reynolds numbers. *AIAA Journal* **37** (9), 1062–1071.

Seifert, A. & Pack, L. G. 2002 Active flow separation control on wall-mounted hump at high Reynolds numbers. *AIAA Journal* **40** (7), 1363–1372.

Sharma, A., Bhaskaran, R. & Lele, S. K. 2011 Large-eddy simulation of supersonic, turbulent mixing layers downstream of a splitter plate. In *AIAA Paper 2011-208*.

Shkurenkov, I. & Adamovich, I. V. 2016 Energy balance in nanosecond pulse discharges in nitrogen and air. *Plasma Sources Science and Technology* **25** (1), 015021.

Sinha, A., Alkandry, H., Kearney-Fischer, M., Samimy, M. & Colonius, T. 2012 The impulse response of a high-speed jet forced with localized arc filament plasma actuators. *Physics of Fluids* **24** (12), 125104.

Strazisar, A. J. & Reshotko, E. 1978 Stability of heated laminar boundary layers in water with nonuniform surface temperature. *The Physics of Fluids* **21** (5), 727–735.

Strazisar, A. J., Reshotko, E. & Prahl, J. M. 1977 Experimental study of the stability of heated laminar boundary layers in water. *Journal of Fluid Mechanics* **83** (02), 225–247.

Tian, H., Ren, T.-L., Xie, D., Wang, Y.-F., Zhou, C.-J., Feng, T.-T., Fu, D., Yang, Y., Peng, P.-G., Wang, L.-G. & Liu, L.-T. 2011 Graphene-on-paper sound source devices. *ACS Nano* **5** (6), 4878–4885.

Vreman, A. W. 2004 An eddy-viscosity subgrid-scale model for turbulent shear flow: Algebraic theory and applications. *Physics of Fluids* **16** (10), 3670–3681.

Vukasinovic, B., Rusak, Z. & Glezer, A 2010 Dissipative small-scale actuation of a turbulent shear layer. *Journal of Fluid Mechanics* **656**, 51–81.

Wiltse, J. M. & Glezer, A. 1998 Direct excitation of small-scale motions in free shear flows. *Physics of Fluids* **10** (8), 2026–2036.

Winant, C. D. & Browand, F. K. 1974 Vortex pairing: the mechanism of turbulent mixing-layer growth at moderate Reynolds number. *Journal of Fluid Mechanics* **63** (02), 237–255.

Wu, J.-Z., Lu, X.-Y., Denny, A. G., Fan, M. & Wu, J.-M. 1998 Post-stall flow control on an airfoil by local unsteady forcing. *Journal of Fluid Mechanics* **371**, 21–58.

Wu, J.-Z. & Wu, J.-M. 1993 Interactions between a solid surface and a viscous compressible flow field. *Journal of Fluid Mechanics* **254**, 183–211.

Yeh, C.-A., Munday, P. M. & Taira, K. 2017*a* Laminar free shear layer modification using localized periodic heating. *Journal of Fluid Mechanics* **822**, 561–589.

Yeh, C.-A., Munday, P. M. & Taira, K. 2017*b* Use of local periodic heating for separation control on a NACA 0012 airfoil. In *AIAA Paper 2017-1451*.

Yeh, C.-A., Munday, P. M., Taira, K. & Munson, M. J. 2015 Drag reduction control for flow over a hump with surface-mounted thermoacoustic actuator. In *AIAA Paper 2015-0826*.

Yeh, C.-A., Sun, Y. & Taira, K. 2017*c* Thermal-based separation control of flow over an airfoil and its resolvent analysis. In *TEFC9-1315*. 9th JSME-KSME Thermal and Fluids Engineering Conference.

Zang, T. & Hussaini, M. Y. 1985 Numerical experiments on the stability of controlled shear flows. In *AIAA Paper 1985-1698*, p. 1698.

Zhuang, M. & Dimotakis, P. E. 1995 Instability of wake-dominated compressible mixing layers. *Physics of Fluids* **7** (10), 2489–2495.